SubPc/C60 Bulk Heterojunction Interfaces Using Illuminated KPFM

by

Ella Phillips

A thesis submitted to the Department of Physics
in partial fulfillment of the
requirements for the degree of
Bachelor of Arts in Physics

May 25, 2025

Approved by

Katherine Aidala, Kennedy-Shelkunoff Professor of Physics, Mount Holyoke College
Alexi Arango, Associate Professor of Physics, Mount Holyoke College
Alan van Giessen, Associate Professor of Chemistry, Mount Holyoke College

Abstract

Third generation solar cells are the future of energy collection and storage. Organic photovoltaics (OPVs) made of layers of organic semiconductors are what make up these solar cells, but the material interfaces are still not something that is fully understood. By doing Kelvin-probe force microscopy scans on the bulk heterojunction interface, we are able to understand more about energy conversion from photons to electricity and what materials allow for the highest efficiency. Creating an ‘open-faced’ solar cell by depositing a donor material, boron subphthalocyanine chloride (SubPc), and the acceptor material, buckminsterfullerene (C60), where then MoO_3 collects holes that go into the ITO substrate, we are able to determine the photovoltage at the heterojunction. Using Kelvin probe force microscopy (KPFM), the interface can be studied to see the energy band offset of the two materials, calculating the potential difference. Our results show that these organic photovoltaics have a difference in potential of 20-30 mV between dark and illuminated scans.

Acknowledgments

Katherine Aidala I would like to thank my advisor Kathy for all of the continued support she has given me during my physics studies at Mount Holyoke. I am so grateful to have been let into the lab starting the summer after my freshman year, as it allowed me to realize my love for materials and understanding the role they can play in helping create clean energy devices. She has been so helpful during the thesis process, and without her guidance this would not have been possible.

Alexi Arango I would like to thank Alexi Arango for all of his help throughout my undergraduate physics studies with understanding solar cells and fabrication of devices. Without his support of our work, we would not have been able to fabricate these samples and understand the implications of them.

Alan van Giessen I would like to thank Alan van Giessen for his support of my thesis work on my committee, as well as his support as one of my professors. I would not be able to understand these materials as well without the help of the chemistry courses I took with him, and I greatly appreciate him being on my thesis committee.

Aidala SPM Lab Both current and former members I have worked with, especially Bea Croteau, Atqiya Zaima, and Icarus Blum for their support through this project, as without them we would not have made it as far as we did on this project. Also, I would like to thank Valentina Flores Montes, Estefania Baca, and Sophia Yuan for giving feedback throughout the research process.

Mom, Dad, and Emery I would like to thank my family for their support, encouragement, and love throughout my academic journey. Their belief in me has been a source of motivation, and I could not have completed this milestone without them.

Contents

List of Figures

Chapter 1:

Introduction

1.1 Solar Energy Motivation

1.1.1 Photovoltaics

Photovoltaics describe the conversion of light into electrical energy, mostly from the Sun's light. These systems and materials are used broadly for energy conversion and storage, but it is currently still more costly than traditional power generation such as burning coal or fossil fuels, making people reluctant to switch to solar energy [1]. Photovoltaic energy helps mitigate climate change because it does not emit greenhouse gases when generating energy. To convert energy from light, semiconducting materials that exhibit the photovoltaic effect must be used.

The photovoltaic effect describes the generation of voltage and current in a material once it has been exposed to light. Light is absorbed into a material, which causes electron-hole pairs to be created that are then separated within the material. An electric potential is then produced by the separation of charges, and this is collected and transformed into electrical energy.

1.1.2 Organic Solar Cells

An organic photovoltaic (OPV) describes a photovoltaic cell, generally a solar cell, that uses organic electronics for its light absorption and charge transport. The organic materials can be an organic polymer or small organic molecule. The materials used in an organic solar cell are less costly than inorganic materials, which allows for them to be fabricated at a large volume. The band gap in organic materials can be changed, allowing for electrical tunability and for more light to be absorbed in a smaller amount of material [2]. Some of the main disadvantages of solar cells include lower efficiency and stability compared to inorganic photovoltaics. The main advantage of organic solar cells is that they are lightweight, able to be fabricated using printed electronics, and can be flexible. They also have the potential to exhibit transparency, which could have future applications in windows or flexible electronics.

OPV is a rapidly growing photovoltaic technology with main research focuses on improving cell efficiency, and increasing the performance lifetime. In its current state, there have been certified experiments with 19.7% efficiency and some with over 10 years of performance [3]. While OPV materials have been around for a while, they have more recently gained attention due to improvements in material design and purification of materials that led to a large increase in the material performance.

Organic molecules are composed of molecules that are weakly bonded by van der Waals forces and because of this, individual properties of the molecules are retained to a much greater extent compared to inorganic materials that form crystalline lattices. Understanding the properties of organic solids is much different than inorganic in this way, as it is necessary to understand the individual properties of the molecules instead of the solid as a whole.

1.1.3 Thin-Film Devices

Thin-film devices describe a range of devices such as solar cells, transistors, and diodes that are made using thin film deposition. The main use for thin-film electronics are for making printed electronics, which allows for a high volume of these electronics to be made at a time in a streamlined process. Thin-film is a layer of materials ranging from monolayer to micrometers in thickness. Thin film deposition is used widely in semiconductor devices, as they play a large role in the development and study of materials with new properties.

Thin-film transistors (TFT) are one of the main types of thin-film devices and they are a type of field-effect transistor (FET). They can be made with many semiconductor materials, and are deposited using chemical vapor deposition, atomic layer deposition, and sputtering. It can also be deposited from a solution using techniques such as spray coating or spin coating.

Thin-film solar cells are another type of thin-film device, made by depositing thin layers of photovoltaic material onto a substrate. They generally have a nano to micron scale thickness. Many emerging thin-film solar cell technologies utilize quantum dots, perovskites, and organics.

1.2 Solar Cell Physics

1.2.1 How Organics Behave in Solar Cells

Organic materials have many differences than inorganic in a solar cell. Due to the structure of organic materials, they tend to have more traps and be more disordered. In inorganic materials, the crystal lattice structure allows for the energy bands to align well, but this is not the same case for organic materials. This causes band bending, where the band structure in a material curves up or down near a junction or interface. This is because the electrochemical potential of the free charge carriers around a semiconductor interface are not similar, and so the charges are transferred between the two materials in a non-linear way [4].

1.2.2 Photon Absorption, Electron-Hole Generation, and Collection of Energy

Photons are emitted from the sun in a variety of wavelengths, primarily from infrared to ultraviolet light. Photons are absorbed through the semiconductor layer of a solar cell, where the chance of absorption changes depending on the material. The photon could pass through the semiconductor, which tends to happen to photons with a lower energy. The photon also has a chance to reflect off the surface of the semiconductor, not being absorbed at all. Photons also can be absorbed by the semiconductor if the photon energy is higher than the band gap value. The key equation that describes a photon's chance of absorption into a solar cell is based on the Beer-Lambert law, stating that the intensity of light decreases exponentially with the depth of penetration into the material. This equation is given below.

$$I(x) = I_0 e^{-\alpha x} \tag{1.1}$$

In this equation, I_0 is the light intensity, I is the transmitted intensity, α the attenuation rate, and x the thickness of the medium. An ideal thickness is on a scale of $1/\alpha$, as this helps account for the absorption of the majority of photons with a particular energy, and thicker devices have a larger series resistance, which decreases the power. This means that fewer photons are collected because the recombination probability increases as the thickness of the material increases.

Once photons are absorbed by the semiconductor in a solar cell, the energy is given to an electron in the valence band. This then excites the electron to the conduction band where it is able to move freely within the semiconductor. Now, there is one fewer electron in this band and there is a positive charge left behind, known as a hole. An example of this is in Figure 1.1.

For a photon to excite an electron from the valence band to the conduction it must have an energy greater than that of the band gap. This can also be described as an electron being excited from the highest occupied molecular orbital (HOMO) to the lowest unoccupied molecular orbital (LUMO), creating an electron-hole pair, or exciton. Excitons are bound by Coulombic attraction between the electron and hole, especially in organic molecules. In organic solar cells, donor-acceptor heterojunctions are often used to separate the excitons, taking advantage of the different energies in the valence and conduction bands. Once an exciton reaches the heterojunction and is in the donor-acceptor material, the hole and electron are further separated which results in a smaller Coulombic force between the particles [2]. For every material there is a distance which a split exciton can travel before recombination

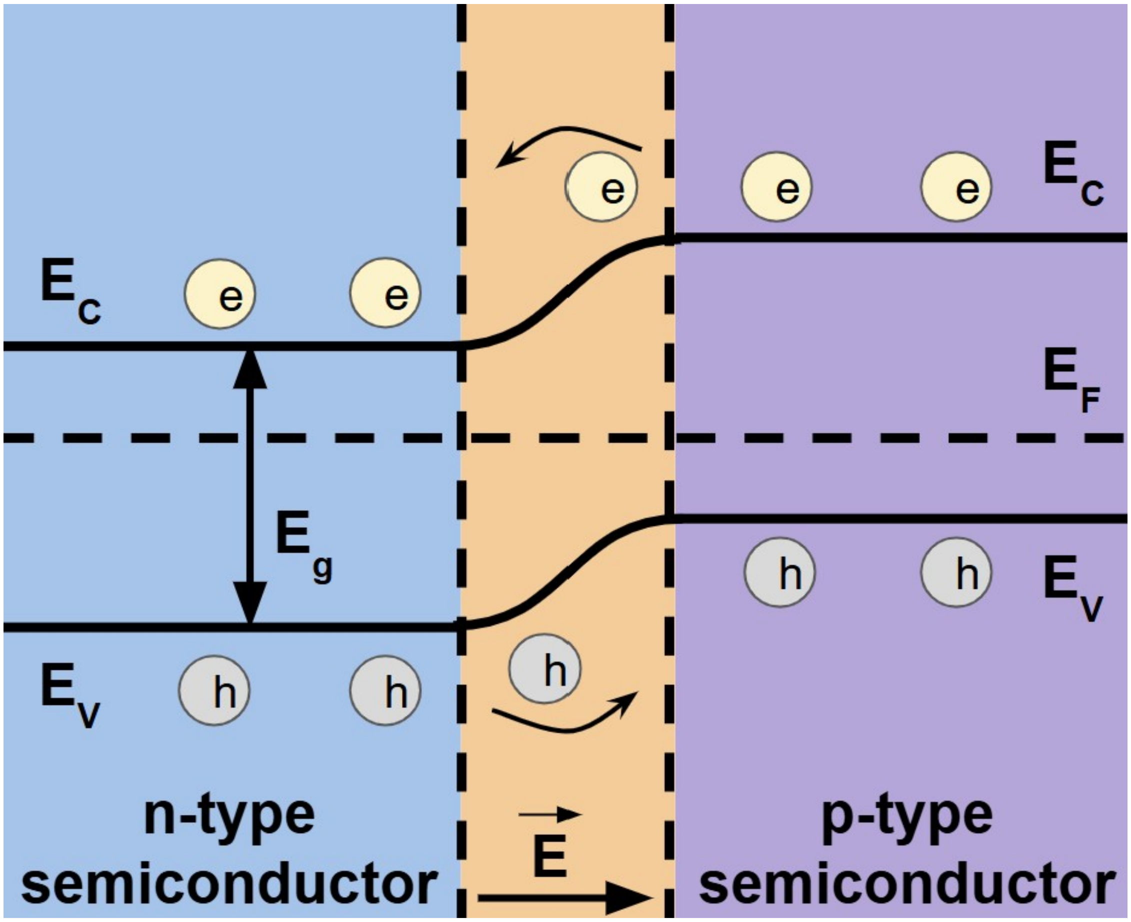

Figure 1.1: Band bending in a p-n junction in semiconducting material.

occurs. If the charges are able to travel to the electrodes, they are collected and used to power a circuit.

1.2.3 Open-Circuit Voltage, Short-Circuit Current, and Efficiency

The open-circuit voltage, or V_{OC}, describes the electrical potential difference between two terminals of a device when it is not connected to a circuit. It represents the maximum voltage that a cell is able to produce. The ideality factor is a parameter that describes how well a diode follows the ideal diode equation, given by the following equation:

$$I_D = I_S(e^{\frac{V_D}{nV_T}} - 1) \tag{1.2}$$

Where I_D is the diode current, I_S is the reverse-bias saturation current, V_D is the voltage across the diode, V_T is the thermal voltage, and n is the ideality factor. The ideality factor gives information about the current conduction or recombination processes occurring inside a device, and it is obtained from the electrical current-voltage relationship.

Short-circuit current (J_{SC}) is the current through a solar cell when the voltage across the cell is zero. Generally, the short-circuit current is the largest amount of current that can be drawn from the cell. It depends on a variety of factors, including the number of photons being absorbed by the semiconductor, the spectrum of the photons, and the optical properties of the cell. The short-circuit current can be calculated using the following equation:

$$J_{SC} = qG(L_n + L_p) \tag{1.3}$$

In this equation, q is the charge, G is the generation rate of charge carriers, and L_n and L_p are the electron and hole diffusion lengths, respectively.

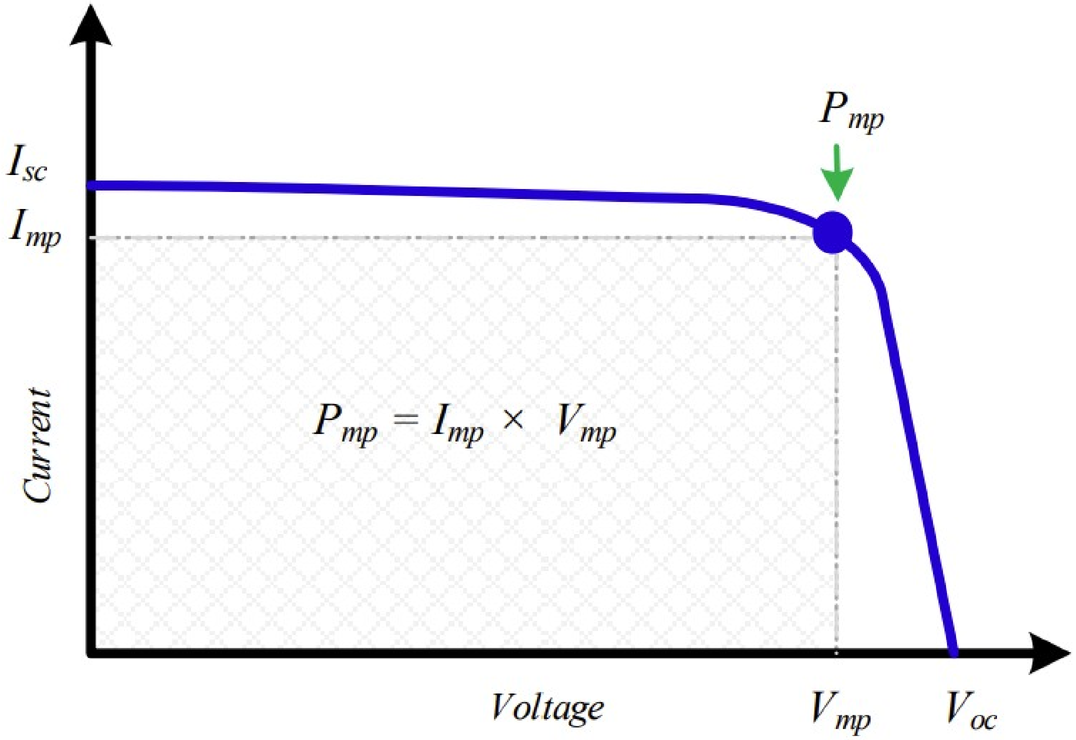

Figure 1.2: I-V curve of a solar cell [5].

The I-V curve graphically shows the relationship between the current produced by the cell and the voltage across it under certain conditions. The conditions used are the short-circuit current and the open-circuit voltage. It shows how efficiently the cell converts sunlight into electricity, with P_{mp} being the maximum power of the cell.

The efficiency of a solar cell refers to the percentage of sunlight that is converted into usable electricity. The fill factor is a measure of how close the solar cell's power output is to its theoretical maximum power. This can be calculated using the solar cells I-V curve, such as that in Figure 1.2. Having a higher fill factor means that a solar cell is more efficient, as it is extracting more power from the light.

1.2.4 Summary of Physics

Overall, these characteristics of a solar cell all come together to define the cell's electrical output. When looking at the theoretical and experimental current-voltage plots, the V_{OC} and J_{SC} are able to provide insight into the theoretical power and see if the cell is performing at its maximum theoretical power.

1.3 Material Interfaces

1.3.1 Why Interfaces of Materials Matter

Material interfaces offer a new way to study the intrinsic properties of a material and how it interacts with other materials. The study of materials interfaces took off in the 1970s due to its use for improving microelectronics, processing, and phase transformations. Interfaces generally fall into three categories, thin-film, semi bulk, and bulk. For each of these interface types, there are different experimental techniques to study them. Bulk material interfaces are generally between thick crystals, semi-bulk material interfaces are generally between thick substrates, and thin film interfaces are generally in superlattices. At a material interface, scientists are able to observe electronic and magnetic properties of materials, which assist greatly in research for microelectronics such as transistors and solar cells [4]. Interfaces significantly influence a materials overall properties and behavior, and by understanding the chemical properties of these interfaces, researchers can use materials with certain properties for specific applications by manipulating the interface.

Optimizing the efficiency of the transfer of energy across the boundary of two different materials and minimizing energy loss is a large part of the study of material interfaces. If the material interface is able to be optimized, then this also helps improve the overall efficiency of a device. Interfaces of energy materials have a large impact on performance and reliability, and the mechanical behavior at these interfaces is closely linked to the structural stability and durability of the materials. Electrical properties of materials are largely influenced by defects at interfaces, which can alter the pathways for electrons, affecting the efficiency and lifespan of a device [4]. The electrical properties of materials can be observed using atomic force microscopy techniques, in this case Kelvin probe force microscopy.

1.3.2 Donor-Acceptor Materials

Donor-acceptor (DA) materials are described as a set of materials made by combining an electron-rich material as the donor and an electron-deficient material as the acceptor. There is a transfer of electrons from the donor to the acceptor, and this allows for the creation of excitons to happen to generate electrical energy.

1.4 Prior Findings of Photovoltage Using KPFM

While prior literature findings of the photovoltage of SubPc/C60 half solar cells is hard to come by, there is still much to be learned from the KPFM findings of other organic material interfaces. The morphology of the materials greatly affects both the charge generation and the subsequent charge transport to the electrodes. Recently, atomic force microscopy (AFM) has been used to resolve the degree and dimensions of the phase separation in bulk heterojunction solar cells, specifically using polymers [6]. KPFM allows the surface potential to be measured on a nanometer scale by using an atomic force microscope.

Previous studies by Klára Maturová at the University of Eindhoven have incorporated KPFM to study poly[2-methyloxy-5-(3',7'-dimethyloctloxy)-p-phenylene vinylene] (MDMO-PPV) and 1-(2-methoxycarbonyl)-propyl-1-phenyl[6,6]C61 (PCBM). The MDMO-PPV:PCBM blend has been studied as a model system for other organic photovoltaic devices, and has been studied for research on other polymer material studies using KPFM. In the study, they focus on both the surface potential before, during, and after the sample has been illuminated. However, before this, the topography of the sample was taken and is shown in Figure 1.3.

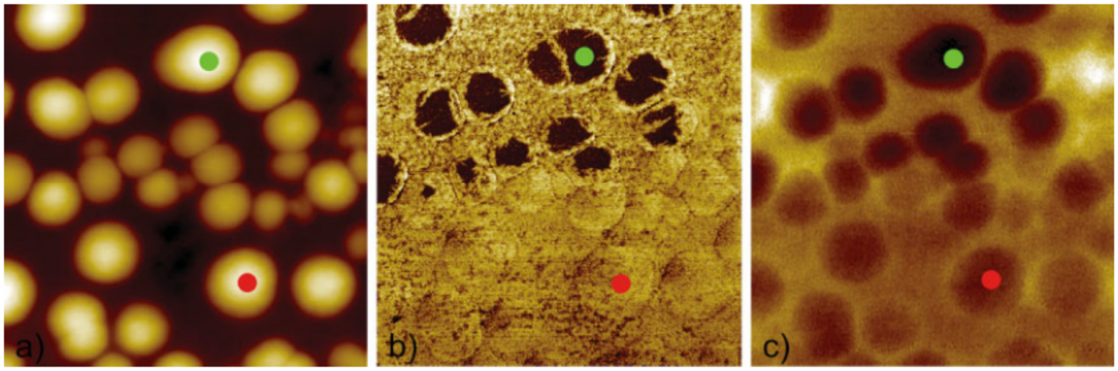

Figure 1.3: AFM-SKPM-images (2x2μm^2)) of a MDMO-PPV:PCBM (1:4 w/w) blend on ITO/PEDOT:PSS a) Topography (total vertical scale 150 nm). b) Phase (70 deg). c) Surface potential (0.1 V). The phase image shows two different types of PCBM clusters: one uncovered (green dot) and one covered (red dot) with a thin MDMO-PPV-rich layer [7].

The contrast between the components of the bulk heterojunctions in dark surface potential images of the blends has been studied, but has not been fully explained. Figure 1.4 below shows the images of the same area as Figure 1.3 above, but under different illumination using KPFM.

The effect of illumination on this specific material blend was found to be a shift in surface potential that is becoming more negative. The shift towards a lower surface potential from in the dark to under illumination indicates an excess of electrons, and the net amount of photogenerated electrons was about equal in both materials making up the heterojunction. Both materials shift in voltage by the same amount, so the darker PCBM clusters can still be seen. In the figure, the color scale shows a) as the brighter area as before illumination

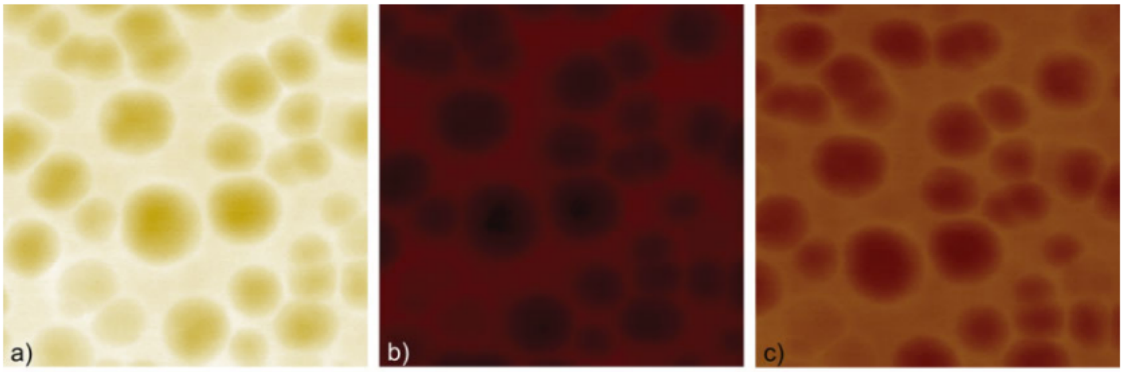

Figure 1.4: Surface potential images of the same area of a MDMO-PPV:PCBM (1:4 w/w) blend (2x2 μm^2, z-range 0.2 V, same scale for all images) on ITO/PEDOT-PSS. a) Before illumination (dark). b) Under white light illumination (light). c) After illumination (dark). Edited from [7].

since there are not photons being absorbed. The absorption of the photons in b) is when the potential shifts to be more negative. After the sample is no longer under illumination, there are still some charges built up on the surface in c) which is why the color is not the same as in a). The researchers also mention that because the bulk heterojunction layers investigated do not allow for a top electrode, there is no built-in electric field through the device. Therefore, surface potential maps are representative of a photovoltaic device under open-circuit conditions, where the current is zero and there is a small electric field. These results prove to be useful for our purposes, since we decided to use their 1:4 ratio of material for our first bulk heterojunction solar cell.

Another study by Qian Zhang at the Weizmann Institute of Science describes photoinduced charge transfer processes between donor and acceptor organic nanocrystals to help develop more efficient materials for photovoltaic applications. They used nanocrystals of perylenediimides for the acceptor material and nanocrystalline copper phthalocyanine as the donor material, and prepared the heterojunctions in different configurations. In configuration I, which we will be focusing on, the CuPc is deposited using physical vapor deposition, which defines the donor-acceptor interface. Similarly to Maturová et al., KPFM measurements of the heterojunction are taken in the dark, but in this experiment the samples were scanned under both laser and LED illumination as well. The results of these scans are shown below in Figure 1.5.

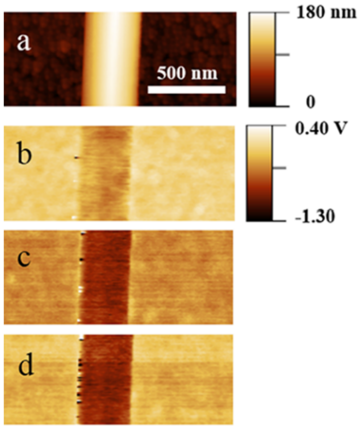

Figure 1.5: KPFM measurements of a PDI ONC on an 80 nm thick CuPc PVD film with EP-PDI. (a) Topography image. (b,c,d) CPD signals in the dark, under laser, and LED illumination, respectively. Edited from [8].

They used the following equation to calculate the photovoltage for both laser and LED illumination:

$$V_{PV} = (CPD_{CuPc} - CPD_{PDI})_{illuminated} - (CPD_{CuPc} - CPD_{PDI})_{dark} \qquad (1.4)$$

Where V_{PV} represents the photovoltage, and CPD_x represents the contact potential difference of the different materials while in the dark or under illumination.

The relative value of the photovoltage is specific to each DA heterojunction, which correlates with VOC in a solar cell. In the dark for the first heterojunction they examined (Figure 1.5b), there is still some contrast in the CPD signal between the areas in the different films. In electron-rich regions where the energy required to move an electron is smaller, there would be a more negative CPD signal. This indicates that the acceptor material accumulates electrons in the dark.

Lastly, in a study by Marco Chiesa at the Cavendish Laboratory, they test the correlation between surface photovoltage and blend morphology. While this is another polymer bulk heterojunction, it tells us about the expected photovoltage values we should see and how the difference in donor and acceptor materials after exposure to illumination. In Figure 1.6, it can be seen that there are 3 distinct areas on the sample surface.

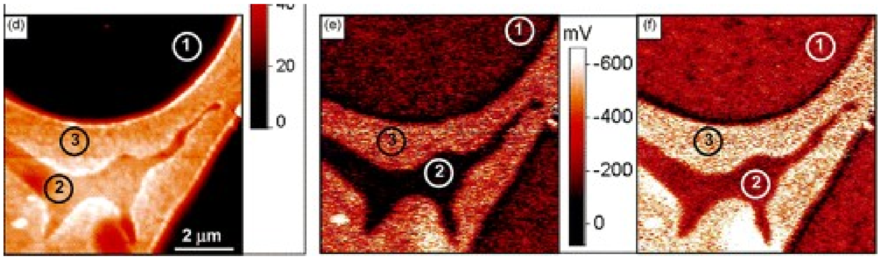

Figure 1.6: SKPM images of thin films of F8BT/PFB blends on top of an ITO anode [9].

The first and third areas, indicated by (1) and (3) are the electron donor and acceptor rich regions. PFB is the donor and F8BT the acceptor, and in the potential scan it is clear that the electron acceptor area becomes more negative than the rest of the sample. It is interesting to note that the entire sample has a shift to be more negative in voltage, but the acceptor area has the largest shift. This was important to keep in mind while we worked on our samples, since this is similar to what we should expect to see and gives us what a general shift in potential could be for a bulk heterojunction in the dark and under illumination.

1.5 Outline of Thesis and Summary

This thesis describes our efforts to fabricate bulk heterojunction solar cells and scan the surface of the interface to see the potential difference between dark and illuminated scans. I will go into detail about the fabrication and scanning techniques used to find the photovoltage of our SubPc C60 solar cells. First, a explanation of the materials used in the device is given, followed by an explanation of Kelvin probe force microscopy and its uses. Our fabrication is compared to prior literature fabrication techniques and findings. Then, the results are shown with analysis and conclusions that we were able to find. Lastly, a summary of the research and our future steps are laid out.

Chapter 2:

Device Techniques and Prior Findings

In this chapter, I discuss the experimental techniques used to fabricate and image our samples. I will first introduce the materials and geometry of our solar cell. In Section 2.2, I explain the imaging techniques that allow us to measure both the topography and surface potential of our samples. Since one of our main goals of this thesis was to determine the fabrication procedure that would allow us to measure the photovoltage, Section 2.4 reviews prior literature and their fabrication parameters.

2.1 Device Structure

2.1.1 ITO Substrate and MoO_3

ITO, or indium tin oxide, is a crucial material in modern solar cells. It is a transparent and conductive electrode, which allows for light to pass through it while still allowing for electricity to flow [10]. The device we use has ITO deposited with a mask onto a silicon glass substrate, and contact is made with the ITO to ground the open-faced solar cell while scanning. The mask acts as a stencil that allows the material to be patterned onto the substrate for precision in the ITO placement.

MoO_3, or molybdenum trioxide, is a inorganic compound with the formula $MoO_3(H_2O)_n$. In solar cells, the interface of MoO_3 and SubPc is used as a blocking layer to prevent electrons from traveling through it to the electrode [10]. At this interface, only holes are able to travel through the MoO_3 which allows for more opportunities for electron-hole splits to occur.

The collection of holes is necessary for electricity to be conducted in the cell, and after the excitons are split they can be collected by the ITO.

2.1.2 Subphthalocyanine (SubPc)

Subphthalocyanine, or SubPc, is a molecule that is composed of a fused cyclic carbon-nitrogen ring system with a boron-chlorine center. The molecular structure of SubPc is shown in Figure 2.1. SubPc has been used in organic solar cells for its optical and nonlinear optical properties as an electron donor. Furthermore, the absorption wavelength of SubPc is more than 94% between 300 to 800 nm, which ensures enough light can be absorbed by this material, and it also has a stable conduction band compared to other materials [11]. The absorption spectra is shown as the red line in Figure 2.2. Efficiencies of up to 6.6% have been seen in perovskite solar cells including SubPc. It has properties that allow for the stability of bulk heterojunctions to increase, since at the interface SubPc can improve charge transport and reduce recombination rates of electron-hole pairs.

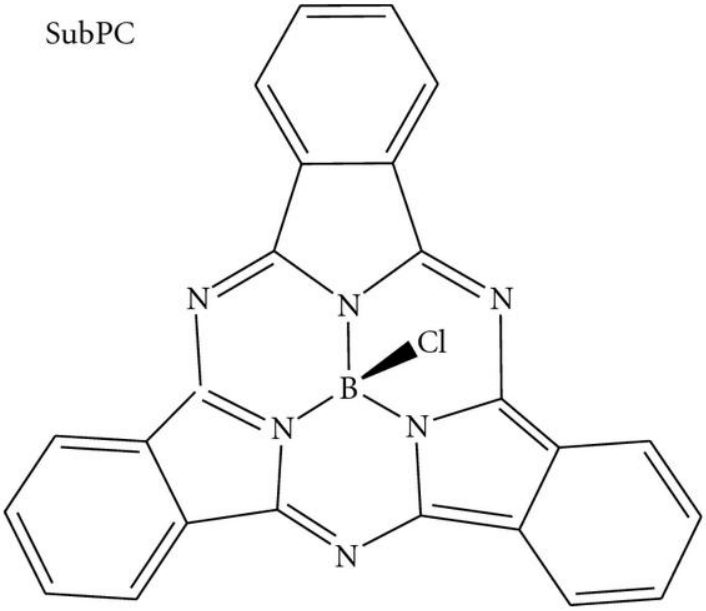

Figure 2.1: SubPc molecule [11].

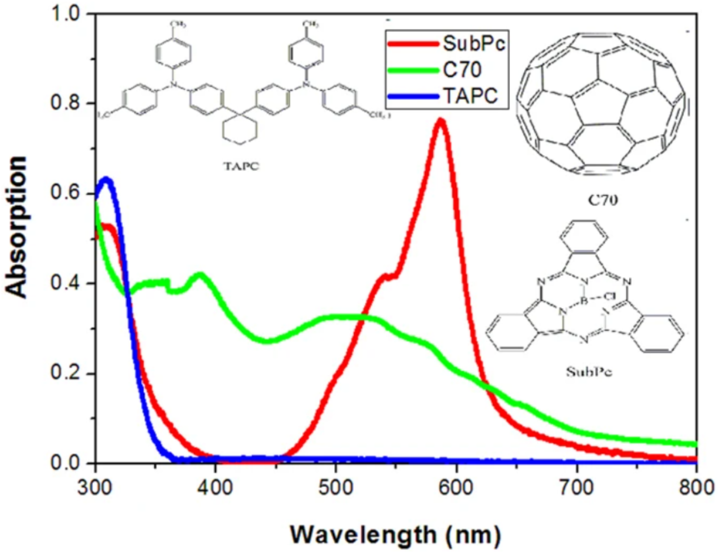

Figure 2.2: SubPc absorption spectrum (red line) [12].

2.1.3 Buckminsterfullerene (C60)

Buckminsterfullerene, or C60, is a molecule that consists of 60 carbons arranged in a truncated icosahedron. The molecular structure of C60 is shown in Figure 2.3. Each carbon atom in the molecule is bonded covalently with three other carbons. Solid C60 forms a brown solid with an optical absorption threshold at about 1.6 eV, and is an n-type semiconductor with a low activation energy of 0.1-0.3 eV. C60 has a very high electron affinity. It is one of the most common electron acceptors in donor/acceptor solar cells, and conversion efficiencies of up to 5.7% have been reported in polymer/C60 solar cells [13].

2.2 Kelvin Probe Force Microscopy (KPFM)

Kelvin probe force microscopy (KPFM) is a scanning probe technique derived from atomic force microscopy (AFM), where the surface potential of a conductive sample can be measured. It is particularly useful in semiconductor and materials research, as it allows for the work function to be measured at the micro- or nanoscale. The AFM consists of a tip at the end of a cantilever that serves as a force sensor, and the topography is imaged by scanning

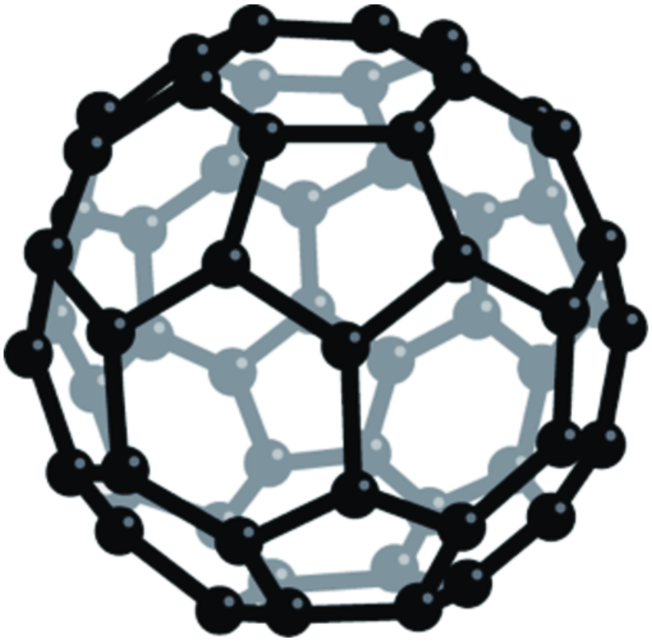

Figure 2.3: C60 molecule [14].

the image across a sample surface while maintaining a constant force by a feedback loop. KPFM works by measuring the contact potential difference (CPD) between a conductive AFM tip and the sample surface. This CPD is the difference in potential between the tip and the sample, which includes charge built up on the surface. Typically, KPFM is viewed as measuring the difference in work function, but it is sensitive to all contributions to the potential at the surface.

2.2.1 AC Tapping Mode

Starting a AFM scan begins with tuning the cantilever to find the resonant frequency of the oscillations of the tip. Tuning is a crucial step for having the correct sensitivity and resolution in a scan. The cantilever acts as a harmonic oscillator, and its resonance enhances sensitivity to small forces. An example of a resonance curve is shown in Figure 2.4.

In AC mode AFM, the cantilever oscillates near its resonant frequency and lightly taps the sample surface to create an image. The probe is only coming into contact with the sample

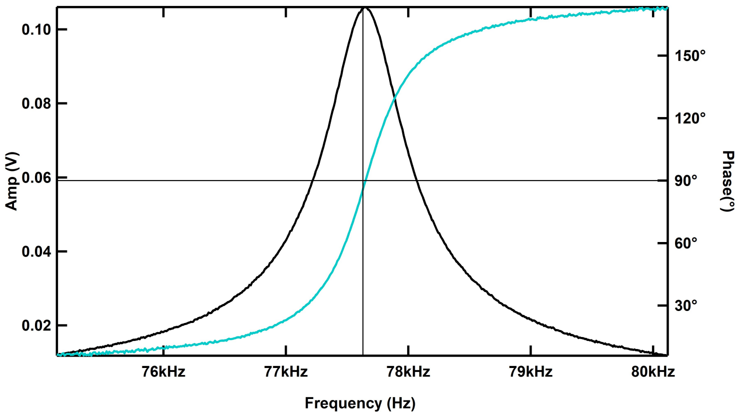

Figure 2.4: Resonance curve taken from AFM tuning. The black line represents the amplitude and the blue line the phase.

surface intermittently, which allows for both the probe and the sample to be preserved for a longer period of time. The oscillation is mechanically excited using a piezoelectric element where the cantilever is mounted, and the forces between the tip and the sample cause a shift in the resonance frequency [15]. An example of the setup for AC mode AFM is pictured in Figure 2.5.

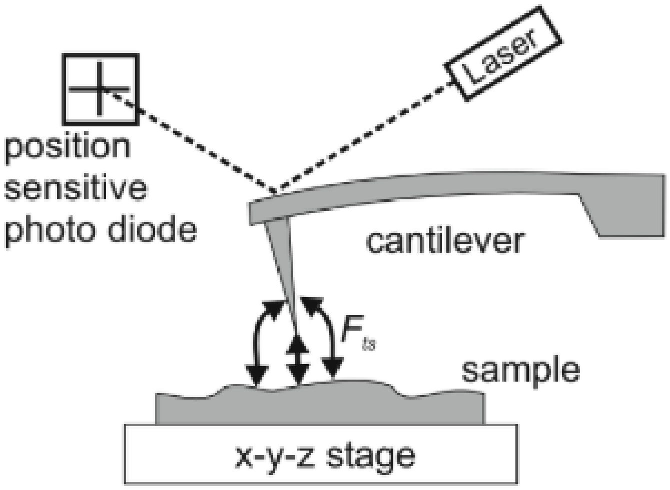

Figure 2.5: Working principle of an AFM consisting of the beam deflection detection system with laser and position sensitive photodiode and the sample on an xyz stage [15].

The oscillation of the cantilever can be described by an equation of motion, where the tip is considered a point-mass spring. The equation can be represented as:

$$m\ddot{z} + \frac{m\omega_0}{Q}\dot{z} + kz = F_{ts} + F_0 \cos(\omega_d t) \tag{2.1}$$

Where k is the spring constant, Q is the quality factor, F_{ts} is the tip-surface interaction, F_0 the amplitude of the driving force, and ω_d the angular frequency of the driving force. The free resonance frequency f_0 also plays a role, as it is a function of the spring constant k and the effective mass m^*, which accounts for the geometry of the cantilever. The equation for this relation is given by:

$$\omega_0 = 2\pi f_0 = \sqrt{\frac{k}{m^*}} \tag{2.2}$$

As the tip approaches the surface, the electric field between the tip and the sample causes there to be some force. This interaction can be caused by short range repulsion, chemical binding force, van der Waals force, and long range electrostatic and magnetic forces. When the tip approaches the sample, the interaction forces will cause a shift in the resonance curve of the cantilever [15].

The feedback circuit is an essential part of atomic force microscopy to ensure a reliable scan, as it determines that the tip has a constant oscillation amplitude. In general, as the tip goes over a bump there is a change in the height of the tip that is detected, and this is sent to the computer to show the plot. In more scientific terms, the piezoelectric actuator drives the cantilever near its resonant frequency, and this is detected using a laser that is reflected off of the cantilever onto a position-sensitive photodiode. An analog signal representing the cantilever's deflection is then produced. This signal is sent to a preamplifier and filtered to remove noise and extraneous signals. Then an amplifier is used to extract the amplitude of the cantilever's oscillatory response to the drive frequency, which is compared against a setpoint that represents the desired oscillation amplitude. The difference between the measured amplitude and setpoint creates an error signal related to the tip-sample interaction, which is processed by the proportional-integral-derivative (PID) controller. The proportional term provides immediate correction to the error magnitude, the integral term accumulates past errors to eliminate steady-state offsets, and the derivative term predicts future error by considering the error's rate of change [15]. The combination of these error corrections allows for the setpoint to be maintained, and preserves image resolution and sample life.

2.2.2 Potential Difference and Photovoltage

2.2.3 Standard Dual Pass KPFM

Dual pass KPFM, also known as amplitude-modulated (AM) KPFM, is the standard technique for Kelvin probe measurements. By electrically exciting the tip of the cantilever by applying an AC voltage that constantly changes sign at the resonant frequency, we are able to measure electric forces. We do this first by finding the topography of a sample, and then a second pass that is lifted off of the surface to avoid short range forces measures the potential difference. In more detail, the potential difference is measured by detecting the electrostatic force between the cantilever tip and the sample by applying an AC voltage and measuring the cantilever oscillation amplitude. The AC voltage regularly changes the sign of the charge on the tip, so the tip is alternately attracted and repelled from the surface. The topography and CPD measurements are decoupled in this mode; first a topographic contour line is recorded in a tapping mode and then the mechanical excitation of the tip is switched off and the tip follows the same contour line shifted in the z direction by a defined height. This allows for the electrostatic response to be decoupled from any other short-range forces that act on the tip during the tapping motion [15].

The electrostatic force on a tip can be calculated by considering the capacitance, C, of the gap between the cantilever tip and the sample. Using the capacitor's energy $W = \frac{1}{2}C(\Delta V)^2$, the electrostatic force can be derived as the following:

$$F_E = \frac{1}{2}\frac{\partial C}{\partial z}(\Delta V)^2 \tag{2.3}$$

Where z is the distance between the tip and the sample, and the potential difference $\Delta V = V_{ext} - V_{CPD}$. V_{ext} is the sum of all externally applied voltages to the tip or the sample. When the sample is grounded and an external voltage is applied to the tip with AC voltage and a constant bias, $V_{ext} = V_{DC} - V_{AC}\sin(\omega_E t)$. The force can then be divided into a static force (F_{stat}) and two dynamic forces (F_{ω_E} and $F_{2\omega_E}$) as shown in the following equations [16]:

$$F_{stat} = \frac{1}{2}\frac{\partial C}{\partial z}[(V_{DC} - V_{CPD})^2 + \frac{V_{AC}^2}{2}] \tag{2.4}$$

$$F_{\omega_E} = \frac{\partial C}{\partial z}(V_{DC} - V_{CPD})V_{AC}\sin(\omega_E t) \tag{2.5}$$

$$F_{2\omega_E} = -\frac{1}{4}\frac{\partial C}{\partial z}V_{AC}^2\cos(2\omega_E t) \tag{2.6}$$

Equation 2.5 is often referred to as the fundamental equation when describing AM-KFPM. In this mode, a feedback loop that minimizes response amplitude by adjusting V_{DC} is more prone to artifacts in the AC drive signal. Equation 2.5 also shows that the electrostatic force is proportional to the gradient in capacitance.

The contact potential difference between the tip in the sample is found, calculated by finding V_{CPD}. This is important for finding the photovoltage, since this value directly corresponds to the photovoltage measurement. V_{CPD} is calculated using the following equation:

$$V_{CPD} = \frac{\epsilon_F^{tip} - \epsilon_F^{sample}}{e} \tag{2.7}$$

Generally, V_{CPD} describes the difference in Fermi levels (ϵ_F) of the tip and the sample, where e is the elemental charge. In equilibrium, V_{CPD} is generally interpreted as the difference in work functions of the tip and the sample material [16].

2.3 Device Fabrication

The samples are fabricated using a multi-step process, beginning with cleaning the surface, evaporation of materials, and annealing the sample. These processes are described in detail in the following section.

2.3.1 Cleaning the Substrate

To begin, glass substrates with predeposited ITO are used. Beakers (100 mL) labeled for deionized (DI) water, Micro90 solution, acetone, and isopropanol (2-propanol) are used, and the substrates are loaded into a holder to be submerged into the baths. Once submerged, a stopper is put on to disallow dust and other particles to get inside of the beaker. To start the process, the beakers must be cleaned with their respective solution. DI water is used to clean the DI water and Micro90 beaker, and 2-propanol and acetone are used to clean their respective beakers. A small amount of the substance is put into the beaker and swirled around, then discarded into the correct waste receptical. The sonicator is filled with tap water to allow for proper cleaning of the materials. The sonicator is used to speed dissolution by breaking intermolecular interactions, so it helps clean the substrates. The first wash is with the Micro90 solution, so the substrates are submerged with the stopper on, which is about 50mL of solution. This is then put into the sonicator to run for 10 minutes. Once complete, the holder can be removed from the beaker, and samples stay in the holder and are rinsed with DI water. After this, they are put into the DI water beaker and the sonication process is repeated. Next is the acetone wash, so the sample holder is submerged in this beaker and the sonication process repeated here. Lastly, the 2-propanol wash is completed with the same steps as above. However, after the sonication process is complete the samples and holder stay submerged in the solution and the beaker is wrapped in foil and brought into the glovebox. Once in the glovebox, the samples can be removed and dried using a nitrogen gun inside the box, and placed into the containers the samples will be held in. Next is the plasma cleaning step.

To begin the plasma cleaning, first the oxygen tank must be opened and the pressure checked. Since oxygen is a flammable material, the vacuum pump uses a non-flammable oil, which is checked to make sure there is a sufficient amount before each cleaning run. Once the oxygen valve has been turned on, the plasma cleaning process can be started. The samples from the glovebox after the sonication cleaning are brought into the deposition glovebox, where the plasma cleaner and evaporator are. The samples are placed into a glass petri dish face up so that the surface can be cleaned. Before the samples are loaded, the chamber is pumped down to vacuum, which can be a longer process if it has not been used in a while. Then one cycle of oxygen plasma cleaning is run without the substrates to clean the chamber. After this is complete, the chamber can be vented back to the pressure of the glovebox. The substrates are then loaded into the chamber in the petri dish, and the chamber is pumped down to vacuum again. The plasma clean cycle is run and the samples can be removed from the chamber to have materials deposited onto them since they are sufficiently cleaned.

2.3.2 Evaporation of Materials

The evaporation of materials is a process in which crucibles, or boats, of material are heated to a very high temperature where the material vaporizes, and then the evaporant molecules settle on the surface of the substrate. For our research, we were able to change the evaporation chamber to have the ability to co-evaporate, where multiple materials can be heated at the same time and deposited onto the substrate at once. A depiction of an evaporation chamber is shown in Figure 2.6.

To begin the process, the substrates in the glovebox are placed face-down into the sample holder for evaporation with a cover placed on top to avoid any material from getting onto the lid of the evaporator. The amount of material in the boats can be checked visually using a long mirror. If a material needs to be changed or added, a long ball-end hex driver and

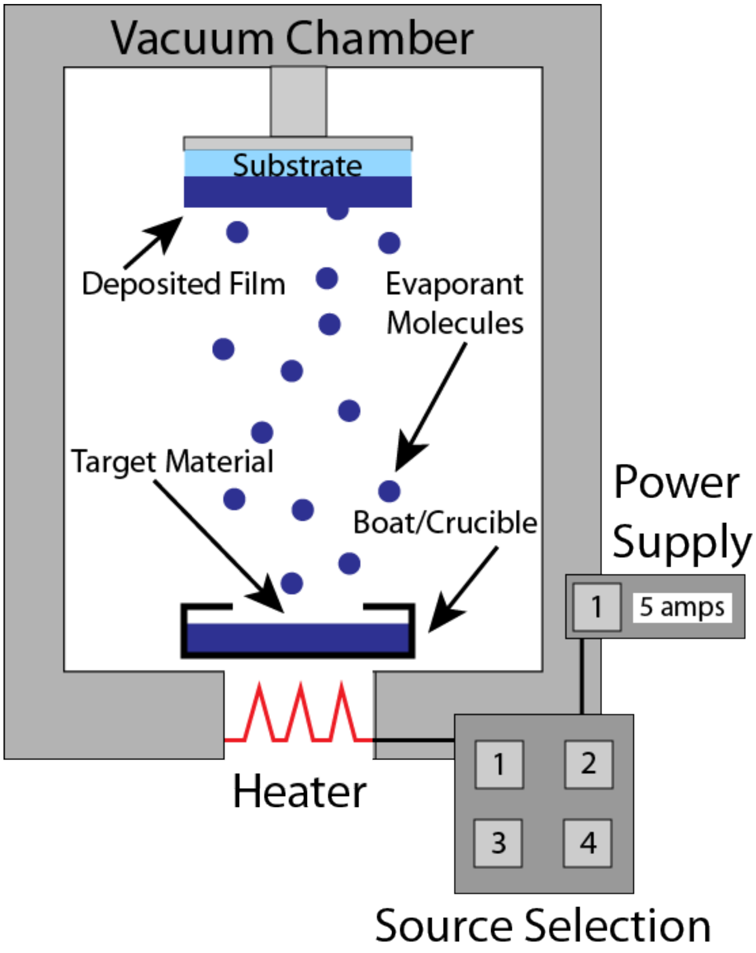

Figure 2.6: Schematic of evaporation chamber.

grabber is used to access the boats. After carefully removing a boat from the chamber while holding it, they can be brought to the main floor of the glovebox. The boat consists of a top and bottom metal piece, which can be separated using tweezers inside of the glovebox. The extra material can be placed into the bottom section of the boat to refill it, and then the top piece of the boat placed back on top with tweezers. This can be picked up with the grabbers and placed back into the bottom of the chamber between the source electrode plates where it was removed, and then tightened again while still holding it with the grabber. Once the bolts are tight, the grabber can be removed from the boat.

Now the evaporation sample holder loaded with substrates and the cover can be placed into the evaporation chamber. The glass lid of the chamber can be closed and tightened and the process to achieve high vacuum can begin. This high vacuum is achieved using a two-stage pump system using a backing pump and turbo pump. The first step to get to high vacuum is to use the roughing pump, where then the two stage pump can be turned on. This is designed to remove large amounts of gas and is used to bring the chamber down to a lower pressure before the more delicate pumps can be activated. The first stage is the turbo pump that is specifically designed to pump at low pressures. It uses high speed rotating blades to achieve vacuum and is directly attached to the thermal evaporator. The second stage of the pump is the backing pump, which is designed to relieve pressure from the back side of the turbo pump. To begin the pump down process, the roughing pump is turned on and left until the chamber reaches 200 mTorr. This is then closed and the backing pump opened, and once the pressure of the chamber and the backing pump stabilize the turbo pump can be turned on. Once the turbo pump accelerates fully, indicated by a green light, the ion gauge can be turned on.

To begin evaporating material, the base pressure must first be below 1×10^{-4} Torr. The source selection must be on the material being deposited, and the film parameters on the thickness monitor must be correct for the desired materials. Ensure that the shutter is closed so that the initial waste material does not get deposited onto the substrates.

The material is preheated, where the current is slowly increased over a span of 2 minutes to 80% of the final current. The current will remain at 80% of the final current for another 2 minutes. After this, the current is slowly increased until it is at 90% of the final current, and then held there for another 2 minutes. Finally, slowly increase the current to the desired final current. The rate of deposition should be relatively constant, and at least 100 $\AA$ should be deposited as waste before the actual deposition begins. After the rate is steady and the waste complete, begin the rotation of the sample holder and open the hatch while resetting the deposited thickness to zero. After the desired thickness of material has been reached, close the hatch and decrease the current back to zero. The rotation of the sample holder can be stopped as well.

To vent the chamber back to glovebox pressure, first the turbo and backing pumps are turned off. These are left off for 2 minutes, and then a quick flush of nitrogen is introduced to the chamber. Wait another 2 minutes before fully opening the nitrogen valve. Once the chamber is able to be opened the nitrogen can be turned off, and the chamber has been vented. It is important to have 2 minutes of waiting after turning off the pumps to allow the turbo blades to slow and the flush of nitrogen to stop the blades since they are very sensitive, and a quick pressure change could break them.

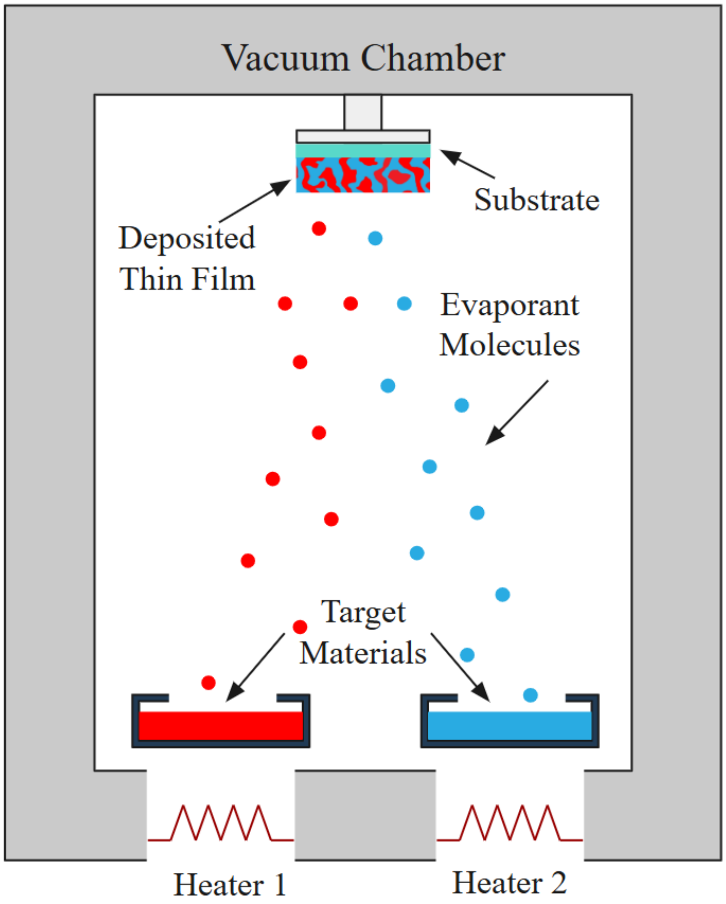

Figure 2.7: Schematic of coevaporation chamber.

Another form of evaporation is co-evaporation, where multiple materials are deposited at once in a evaporation chamber as shown in Figure 2.7. The setup for pumping down and venting the chamber is the same, however, the material deposition is slightly different. The first material to be deposited is the one with a higher ratio in the sample, which should be the one that is registered as the film for the monitor. This is because the evaporation chamber only has one quartz crystal monitor, so only one film setting can be used even though there are two materials being deposited. The quartz crystal monitor is used to measure the thickness and deposition rate of the material being evaporated by programming different film settings for different materials. The current will be brought up to a steady deposition rate following the steps for evaporation, and then the second material can begin the process of getting to the final desired current. Once a steady rate has been reached for the second material as well, the deposition can begin by opening the shutter and rotating the sample holder, similarly to the normal evaporation process. A recommendation is that once the deposition is complete, turn off the first material that was brought up to current and record the material rate that is shown for the second material. This allows for a better estimation of the true ratio of the first to second material. The samples can be removed the same way as in evaporation.

Once the samples have the material deposited onto them, they can be annealed. Generally, annealing is done to improve the structure and properties of the film deposited by the evaporation process by increasing crystallinity, reducing defects, and altering the surface morphology of the film. The samples are returned to the wet deposition chamber and placed on a preheated hotplate at varying temperatures for a varying amount of time, depending on what is trying to be done.

2.3.3 Our Solar Cells

Our solar cells consist of a ratio of SubPc to C60 to make up the bulk heterojunction. They are left without a top electrode, so that the interface of the materials in the bulk heterojunction can be studied. The layers of the solar cell consist of an ITO cathode on glass substrate, a deposited MoO_3 layer to block holes from going into the ITO, and the deposited SubPc/C60 bulk heterojunction. A schematic of our general solar cell we made is shown in Figure 2.8.

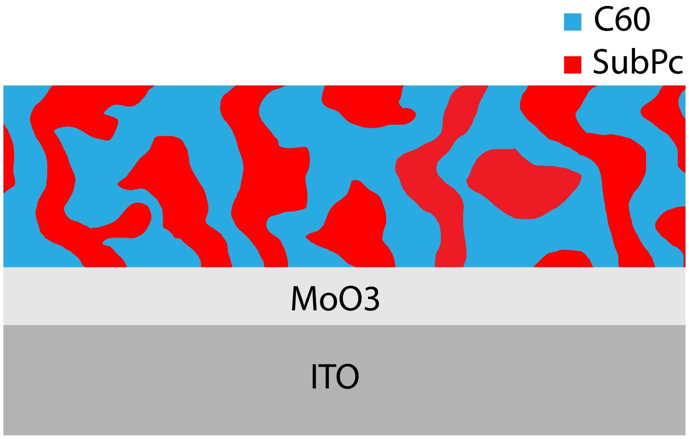

Figure 2.8: Schematic of our solar cell with the ITO cathode, MoO_3, and SubPc/C60 bulk heterojunction.

To begin the fabrication of the solar cells, we start with the glass substrate with pre-deposited ITO, and go through the cleaning process described in the above section. For the evaporation of materials, 100 $\mathring{A}$ of MoO_3 is deposited to be the hole transport layer in our solar cell, connecting the ITO to the SubPc. Then, evaporation of the SubPc and C60 materials can be done. We have done a variety of ratios of SubPc to C60, and we have also created a bilayer solar cell without a top electrode to test the potential that we get compared to the bulk heterojunction solar cell. The first ratio we tested was a 20 % SubPc to 80 % C60 bulk heterojunction, since this was similar to what was seen in literature. We also tested a 40 % SubPc to 60 % C60 heterojunction, and a bilayer solar cell with 200 $\mathring{A}$ of SubPc and 400 $\mathring{A}$ of C60 deposited through evaporation. For the bulk heterojunction solar cells, a total of 600 $\mathring{A}$ of material were deposited. All of the samples were then annealed at 120 $^\circ C$ for 30 minutes.

2.4 Previous Literature

We chose our initial fabrication procedure based on prior literature of devices using either a small molecule/C60 blend or a polymer/C60 blend of materials. We want to generally find the best morphology for our devices, as well as finding the best fabrication technique to achieve the best results using steps like annealing. The deposition thicknesses for SubPc and C60 were chosen based on data from Kim [18], Mutolo [19], and Peet [20] provide fabrication techniques that we used for this thesis. Unfortunately, more work has been done on polymers rather than small molecule blends, so many of the sources are from polymer/C60 experiments.

2.4.1 Thickness of Organic Materials Layers

SubPc thicknesses were chosen based on values from [18], where they studied the effect of different SubPc thicknesses in a SubPc/C60 photovoltaic cell. Kim provides an excellent review on testing different thicknesses for a constant C60 value in solar cells. They kept the thickness of C60 constant for this test, 350 $\mathring{A}$. The SubPc values range from 10 $\mathring{A}$ to 250 $\mathring{A}$, with the optimal value for V_{OC} being 160 $\mathring{A}$ of material, while the optimal value for J_{SC} was 130 $\mathring{A}$. The plot and table of the different values tested are shown in Figures 2.9 and 2.10, respectively. Coevaporation is the standard for bulk heterojunction solar cell deposition, and is utilized in our solar cells.

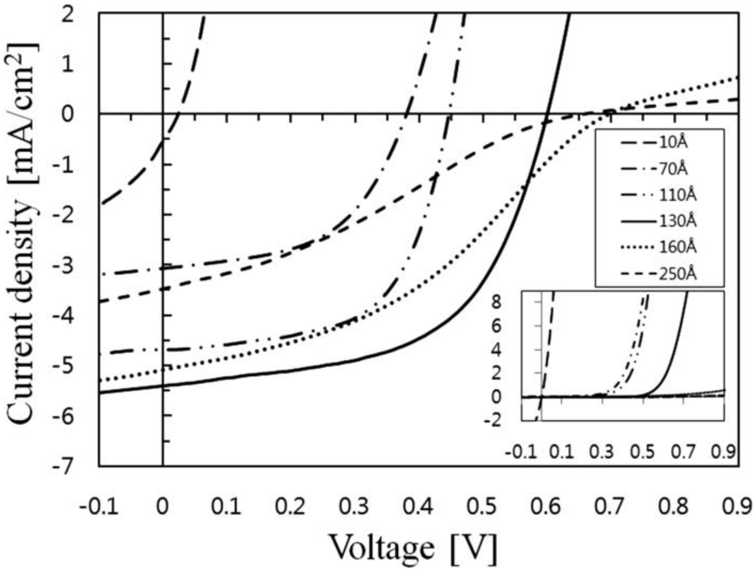

Figure 2.9: Current density vs. voltage (J-V) characteristics of the cells with various SubPc layer thicknesses, d, of 10, 70, 110, 130, 160, and 250 $\mathring{A}$. The photocurrents were measured under an AM 1.5 solar illumination of 100 mW/cm^2. The inset shows the J-V characteristics of the cells in the dark [18].

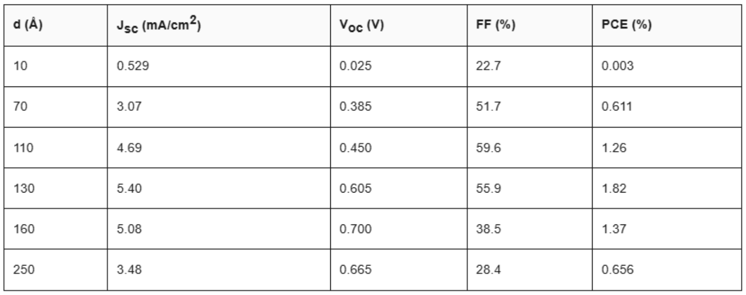

d (Å)	J_{SC} (mA/cm^2)	V_{OC} (V)	FF (%)	PCE (%)
10	0.529	0.025	22.7	0.003
70	3.07	0.385	51.7	0.611
110	4.69	0.450	59.6	1.26
130	5.40	0.605	55.9	1.82
160	5.08	0.700	38.5	1.37
250	3.48	0.665	28.4	0.656

Figure 2.10: Summary of the SubPc/C60 based OPV cell parameters according to the SubPc layer thickness (d) [18].

These were full bilayer cells, where they utilized an ITO/PEDOT:PSS/SubPc/C60/BCP/Al structure. Since these are not bulk heterojunction cells, the ratio of SubPc to C60 will not be exactly what we are replicating for our bulk heterojunction cells but informs us of realistic values for bilayer cells.

2.4.2 Fabrication Techniques

The description of fabrication of a SubPc/C60 solar cell is found in the supporting information in the work of Mutolo [19], where they describe their cleaning process of the substrates using solvents and a UV-ozone treatment prior to deposition. The SubPc and C60 were purified by sublimation prior to use, which was not something that we did in our fabrication steps. They deposited SubPc at a rate of 1 $\mathring{A}$ per second for 130 $\mathring{A}$ and C60 at a rate of 2 $\mathring{A}$ per second for 325 $\mathring{A}$, giving a 2:5 ratio of SubPc to C60. The materials were deposited separately to create a full solar cell.

In another study by Peet [20], they describe the self-assembly of bulk heterojunction materials by spontaneous phase separation. While they do use a polymer C60 blend, they describe their thermal annealing process that leads to better order within the polymer and a demixing of the blend. They also use solvent annealing that had shown to increase performance by allowing control over the molecule packing and fullerene phase separation during the film formation process. Not only did they show that thermal annealing improved the carrier lifetime and mobility through improved morphology, but it also increased the fraction

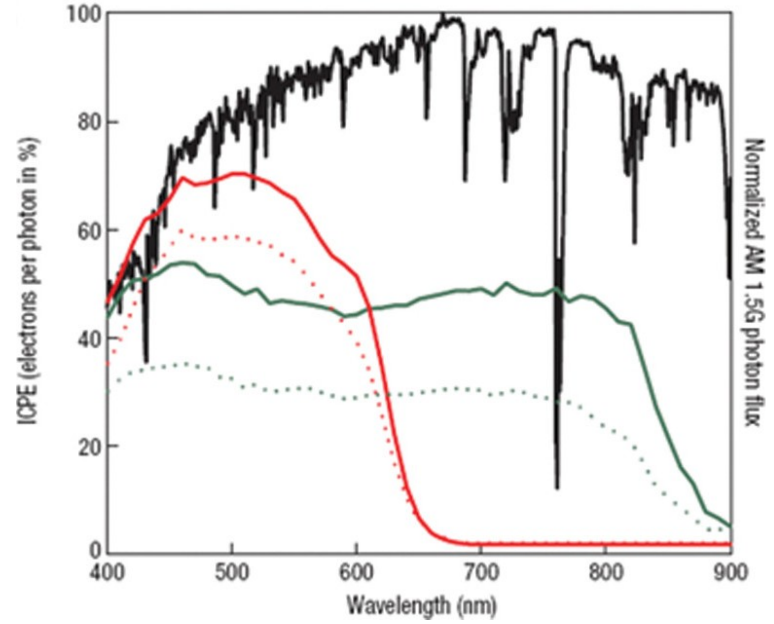

Figure 2.11: EQE specra of solar cells composed of P3HT/$PC_{61}BM$ before (dotted red line) and after (solid red line) thermal annealing. The AM 1.5G solar spectrum is shown in black for reference [20].

of mobile carriers. This is shown in Figure 2.11, where the annealed solar cell (solid red line) shows a higher amount of electrons per photon than the unannealed solar cell (dotted red line). The annealing process having such an effect led us to anneal our samples in an attempt to increase the performance of our heterojunction.

A study by Shahiduzzaman [21] describes an interesting material deposition technique, alternating between perovskites to achieve intercalation of materials. They found the highest efficiency by having four double layers of deposition. Early attempts to fabricate our solar cells used this technique because we previously did not have the capability for coevaporation. In the beginning stages of this project we used this method with annealing to create an interface similar to a bulk heterojunction. These samples are not included in the thesis. They also found that having two double layers of material yielded a higher voltage than that of coevaporation, as shown in Figure 2.12.

From this result, before we had the ability to do coevaporation we did two double layers of alternating SubPc and C60 materials since this theoretically had a higher voltage

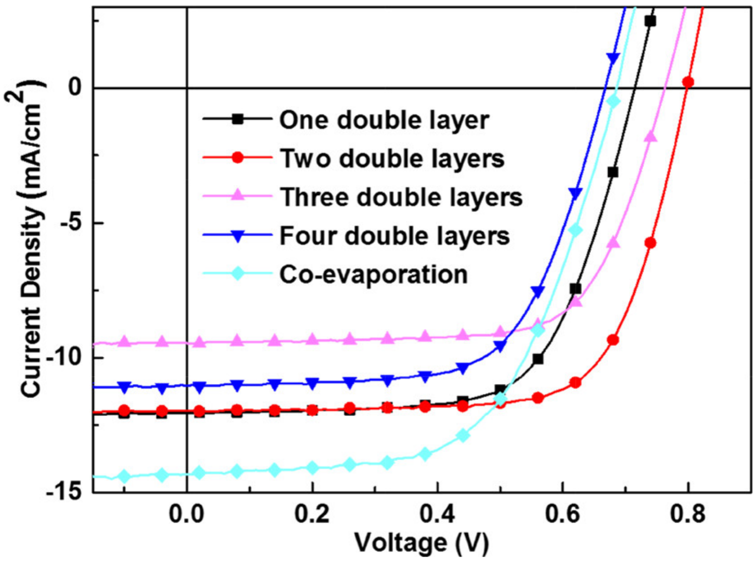

Figure 2.12: Current density-voltage (J-V) characteristics obtained for the devices with a different number of double layers.

than the other number of layers, even though it had a lower J_{SC} value. In most literature, coevaporation is the most common way to create bulk heterojunctions so we used this once we had the ability to coevaporate.

To compare this to the work from Peet [20], Shahiduzzaman [21] also gives a incident current to photon (IPCE) spectra for the differing amount of double layers, as shown in Figure 2.13. It can be seen from this plot that coevaporation gives the highest percent of photon to current conversion efficiency. Using this information in combination with the annealing information allowed us to make a decision to anneal after making these cells.

2.4.3 Improvements to be Made

From reading prior research, it is clear that there are still improvements to be made with our solar cells, and more specifically with our bulk heterojunction. While we would like to reproduce the morphology actually used in solar cells, we are optimizing for spatial measurements, which might lead to a different choice. Varying the annealing temperature could lead to further improvement of charge carrier mobility in our cells, but finding an upper limit of time and temperature is necessary to prevent unwanted changes that could decrease the

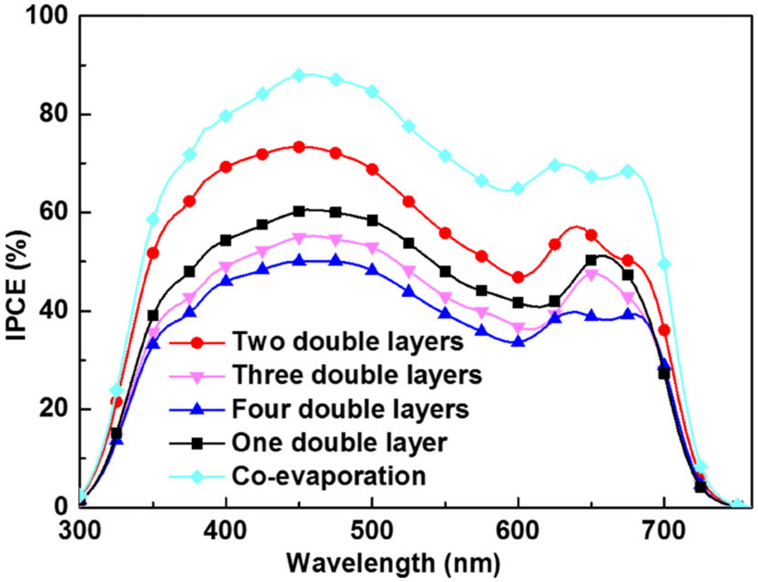

Figure 2.13: IPCE spectra for one to four double layers and for the coevaporated film [21].

performance of the cell. Furthermore, testing different combinations of materials and ratios of SubPc to C60 could be useful in finding results.

Chapter 3:

Results and Discussion

The solar cells were fabricated in the Arango Lab, and a variety of these open-face solar cells were tested using KPFM. The KPFM scans consist of both topographic and potential data, and the overlay of this data can be useful when analyzing the photovoltage measurements. Scans were taken in both dark and illuminated conditions, along with scans in which the sample was illuminated in the middle of the scan in an attempt to see a more obvious potential change. The results were not what we expected, so the focus is on troubleshooting in both topographic and potential scans and a discussion of the results.

A comparison of the bilayer, 20:80, and 40:60 ratio solar cell scans is needed to properly see the effect of light on the potential of the samples. The topography of the samples plays an important role in evaluating the potential, since we want to be able to identify each of the materials. Another important aspect of imaging the surface is the phase of the sample. The phase scan tells the user the shift in resonance, but can also be used to determine different materials. In this case, finding out that there are in fact multiple materials on the surface was an important goal with our phase scans. Since the materials have different mechanical properties, they will have a different phase angle and show up differently in the scan.

The photovoltage, or potential, tells us a lot about the materials and how they interact with illumination. By understanding the potential of the materials when in the dark and under illumination, it allows for solar cells to be designed to capture a larger amount of photons and then generate more energy at a higher efficiency.

3.1 Bilayer Sample

The bilayer sample plays an important role in topography, as it sets a baseline for how smooth one layer of material should be. The scan of the bilayer topography is shown in Figure 3.1. In this figure, we can see that the surface is relatively flat, with the surface consisting of features around 4 nm in height. This is also shown in the line plot across the surface as shown in Figure 3.2.

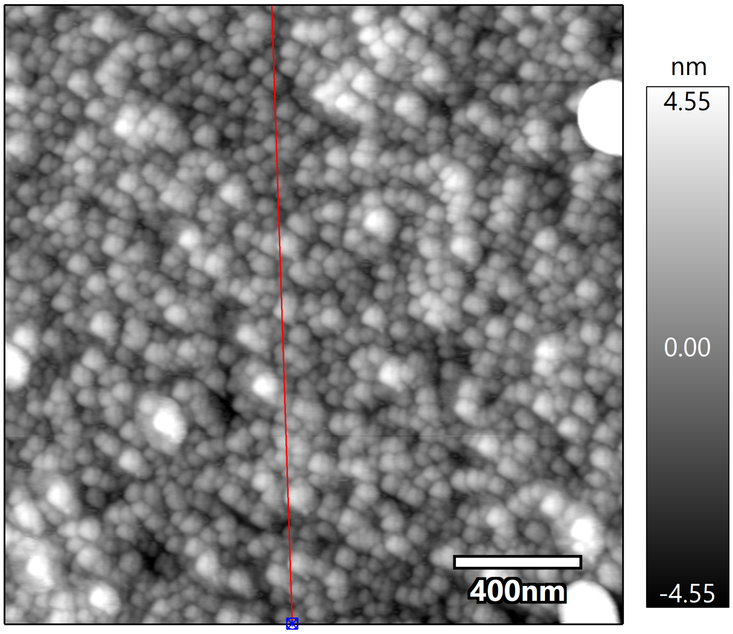

Figure 3.1: Topography of the bilayer sample. Red line indicates where the line plot in Figure 3.2 is taken.

The phase of the bilayer solar cell also plays an important role in understanding the surface of the sample. The phase of the bilayer stays mostly consistent, with a angle of around 68 degrees. There are some spikes in the phase, which indicate pits, or gaps, in the material. This consistent phase indicates that the surface is made mainly of one material, the C60. Figure 3.3 shows the phase of the surface, while Figure 3.4 shows the plot of the phase along the red line. In the plot of the phase, it can be seen that the phase angle changes by about 4 or 5 degrees. The particularly high phase shown in the line plot is associated with

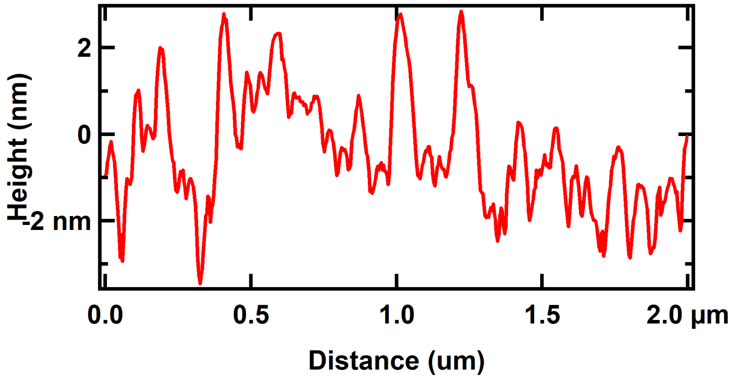

Figure 3.2: Line plot of the topography of the bilayer sample.

pits, and are more likely due to interaction with the topography than indicating a different material.

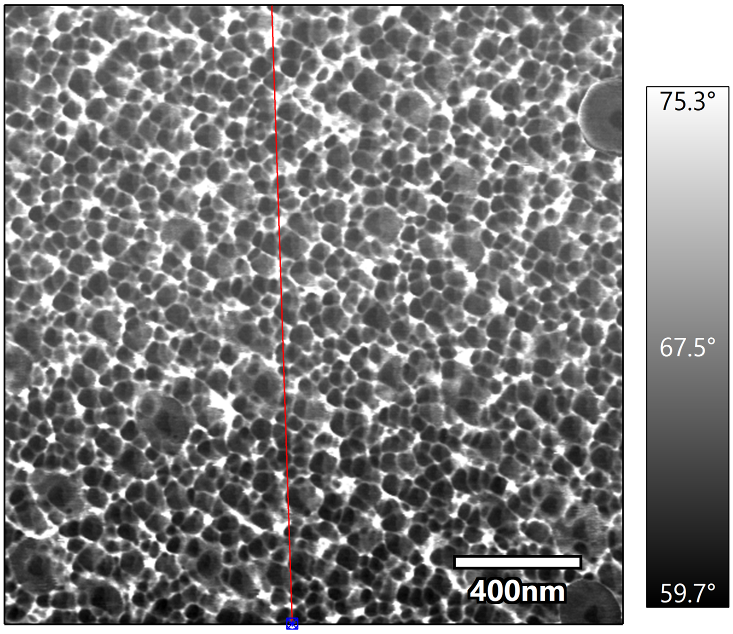

Figure 3.3: Phase of the bilayer sample. Red line indicates where the line plot in Figure 3.4 is taken.

The bilayer solar cell is the first that we imaged to understand the difference between the dark and illuminated potential. In a test, we began our KPFM scan in the dark for a third of the scan, then turned on the light for another third, and then turned off the light

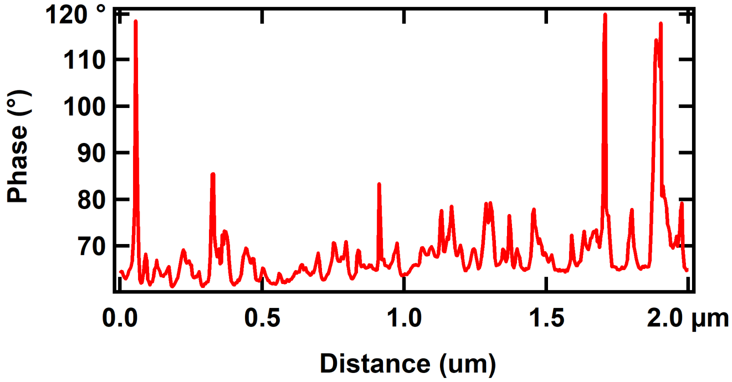

Figure 3.4: Line plot of the phase of the bilayer sample.

again for the last third of the scan. The results were somewhat surprising, and are shown in Figure 3.5, with the plot across the surface in Figure 3.6.

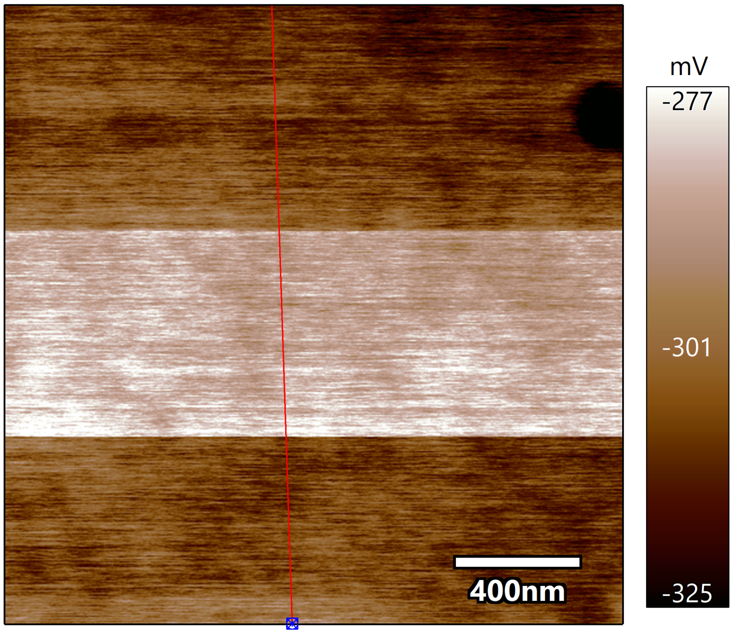

Figure 3.5: Potential of the surface in the dark (bottom third), under illumination (middle third), and after illumination (top third).

It is clear that the potential does shift when exposed to light, but an interesting thing to note is that it shifts in the more positive direction. A little after 0.5 μm, the potential shifts from around -0.305 V to around -0.28 V, which was very unexpected. The difference between the dark and illuminated potential is also only about 30 mV, which is low compared

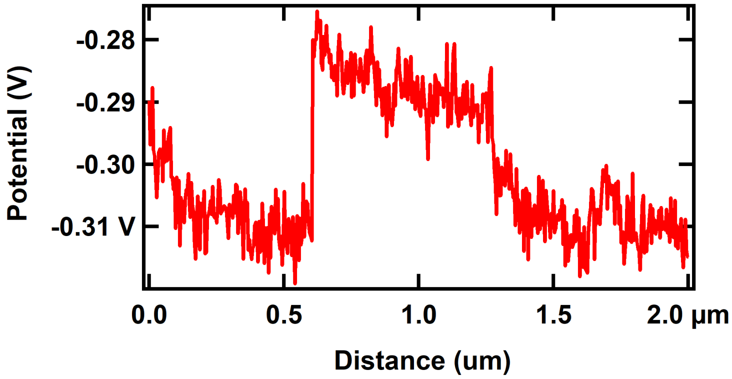

Figure 3.6: Plot of the potential of the surface in the dark (left third), under illumination (middle third), and after illumination (right third).

to what we should have seen. C60 is an acceptor material, so we would expect to see a shift in potential to be a more negative voltage when exposed to light. This will be analyzed further in the discussion, but it is important to note since it is seen in many of the potential scans.

3.2 20:80 Ratio Sample

The 20:80 ratio sample of SubPc/C60 topography shows how different ratios of the material appear when coevaporated together. Figure 3.7 shows the topography of the sample, while Figure 3.8 shows the plot of the line through the topography image. In the topography of the sample, there is a bit more variation in the height that can be seen in the line plot. The topography has more pits than aggregates of material, but the aggregates have a height of around 4-6 nm which leads us to believe that these are clumps of C60.

The phase of the 20:80 bulk heterojunction sample helps us to understand how the materials are spread across the surface of the sample. The phase has some differences than that seen in the bilayer sample, which indicates that there are two different materials on the surface. Figure 3.9 shows the phase of the surface, while Figure 3.10 shows the plot of the phase along the red line. The phase, while it does change, is still not by a significant amount.

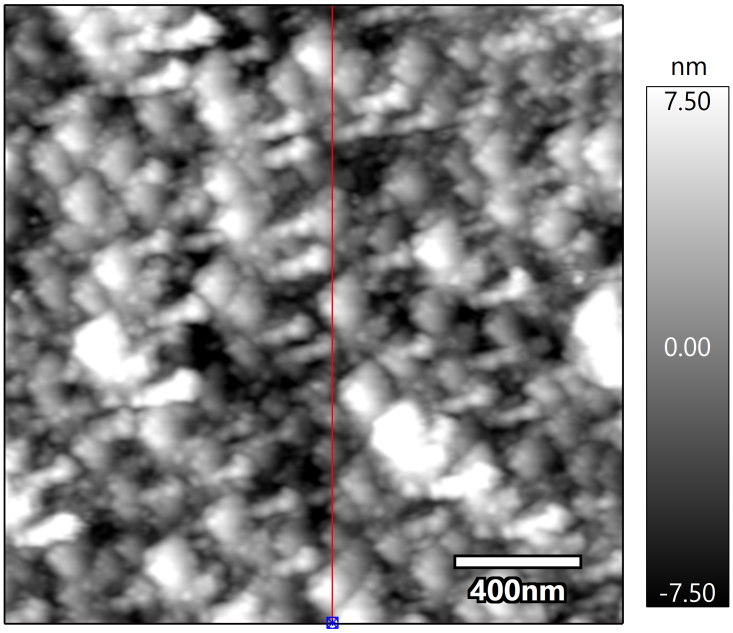

Figure 3.7: Topography of the 20:80 sample. Red line indicates where the line plot in Figure 3.8 is taken.

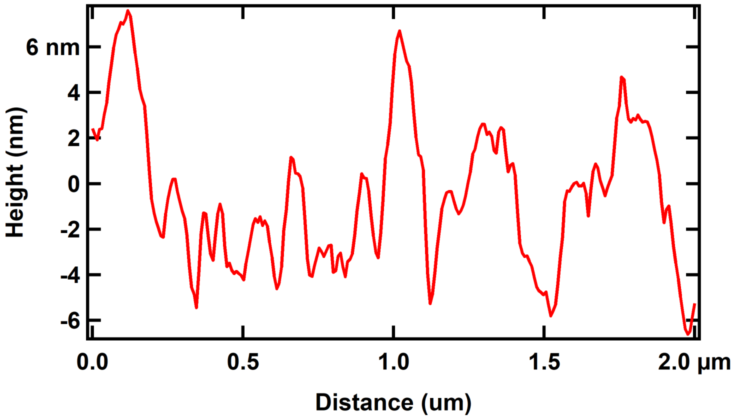

Figure 3.8: Line plot of the topography of the 20:80 sample.

This indicates to us that a larger ratio of SubPc to C60 is needed to see the topography we are hoping for.

Since we saw a slight voltage shift in the bilayer sample, the 20:80 sample was the next to be tested. The results from Maturová showed promise with a 1:4 ratio [7], and this was the next sample we had fabricated. The results are shown in Figure 3.11, with the plot of

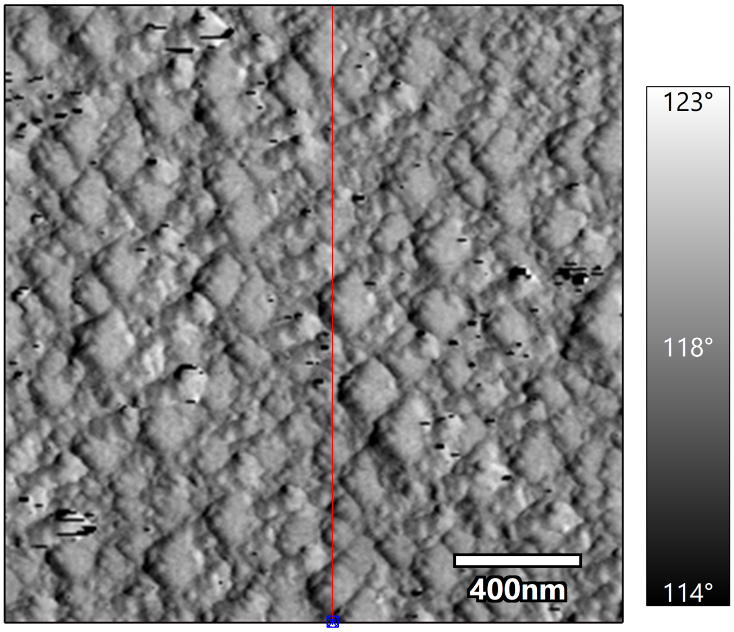

Figure 3.9: Phase of the surface of the 20:80. Red line indicates where the line plot in Figure 3.10 is taken.

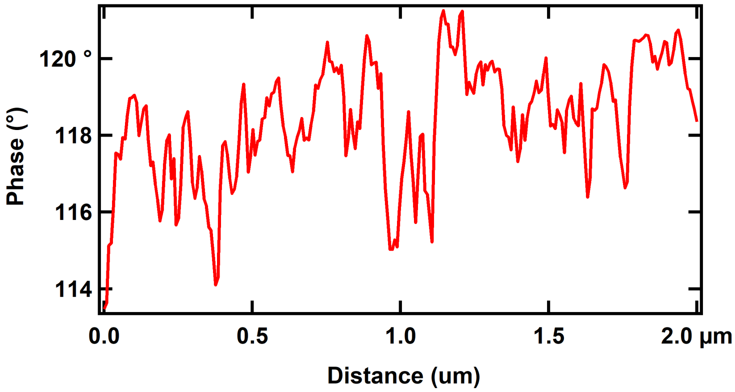

Figure 3.10: Line plot of the phase of the 20:80 sample.

the potential shown in Figure 3.12. For this test, the sample was scanned separately in the dark and under illumination to see the potential difference between them.

The first thing to consider when looking at these plots is the quality of the scan. This scan had some issues that arose, as shown by the large streaks in the image. These streaks are a result of user error while taking AFM images, and are often hard to get rid of while preserving the image integrity. To reduce the amount of these large shifts in potential in these images, a flatten order 0 was applied to the image while masking the darker areas.

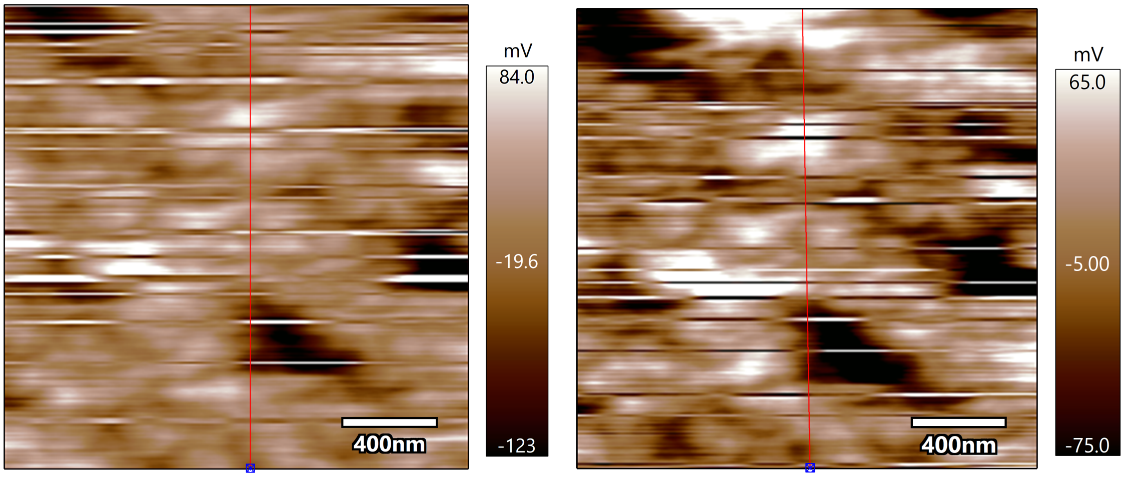

Figure 3.11: Potential of the surface in the dark (left) and under illumination (right).

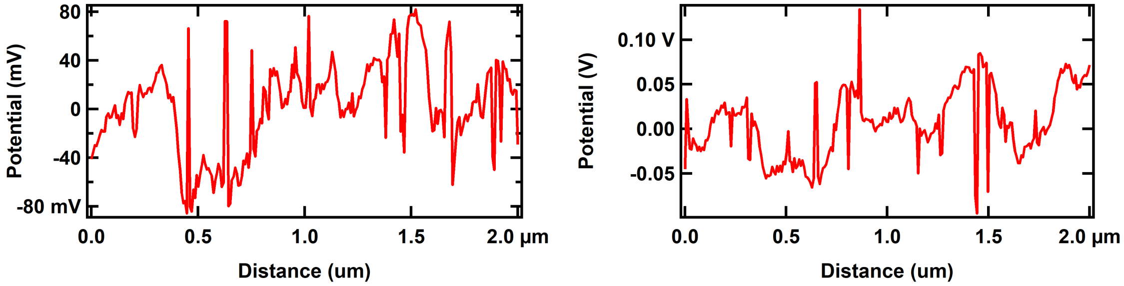

Figure 3.12: Plot of the potential of the surface in the dark (left) and under illumination (right).

Keeping this in mind, there are some real changes in potential, which could correspond to changes in the topography seen in the previous plots. These changes in potential are only about 20 mV, which is interesting since the bilayer sample potential changed by about 30 mV.

3.3 40:60 Ratio Sample

The last sample tested was the 40:60 sample, which was tested after the 20:80 was not showing as much change in the photovoltage as expected between the dark and light scans. One of the tests done for a sample was having the 40:60 sample in the dark and then illuminated, and the topography is shown in Figure 3.13. In this topography it is unclear where the light was turned on, and this is due to the topography of the sample not being impacted by illumination. We see a larger difference in height, with the surface full of taller bumps. We believe this is the C60 clumping together more at this ratio. A plot of the topography through the red line in the figure is shown in Figure 3.14. In this plot, there are two higher aggregates of C60 and one shorter in height. This shorter aggregate we believe was covered by SubPc, which becomes more apparent in the potential scan.

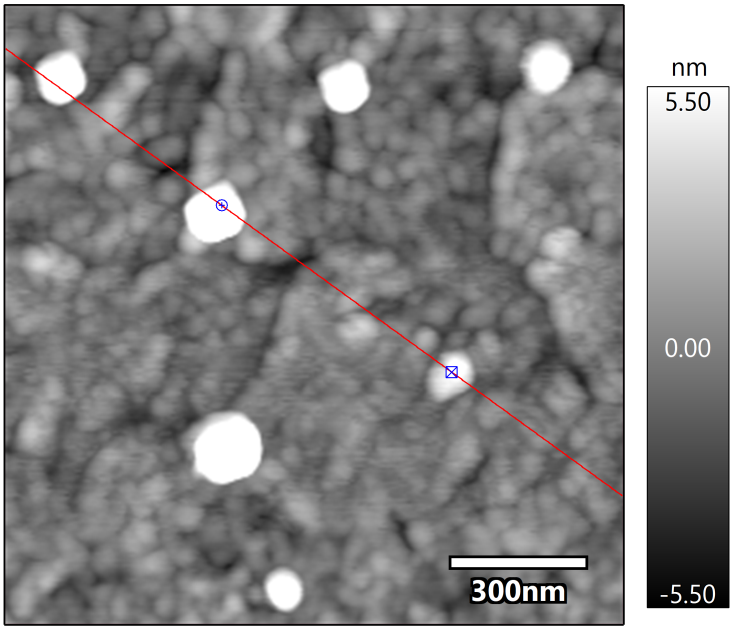

Figure 3.13: Topography of the 40:60 sample. Red line indicates where the line plot in Figure 3.14 is taken.

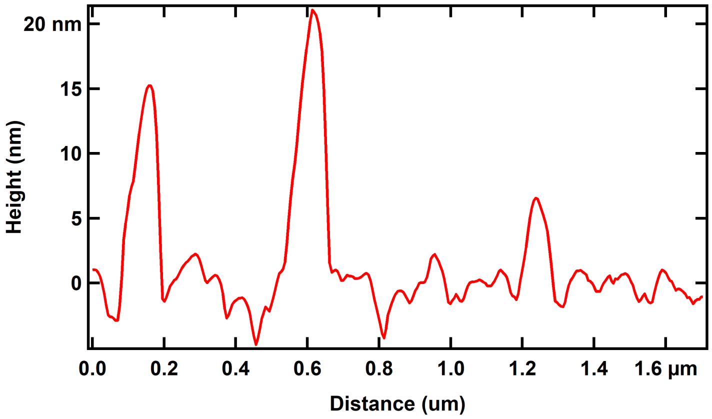

Figure 3.14: Line plot of topography of the 40:60 sample.

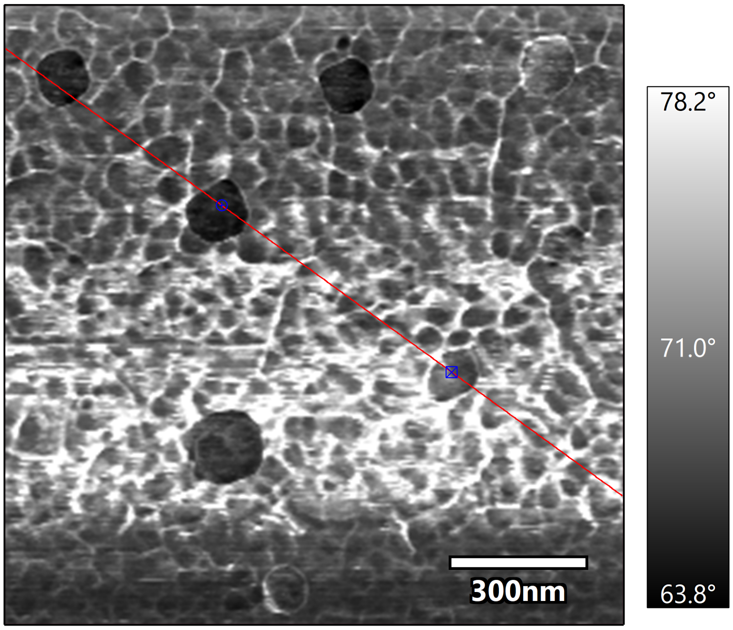

Figure 3.15: Phase of the 40:60 sample. Red line indicates where the line plot in Figure 3.16 is taken.

The surface scan of the phase is shown in Figure 3.15, while the plot of the line is shown in Figure 3.16. The phase shows 4 very distinct aggregates of C60, with a smaller fifth aggregate in the middle right of the image where the line runs through it. This smaller aggregate does show some difference in phase, however, it is not as large of a difference as the other two aggregates on the line plot. We believe that this is because it has a layer of SubPc on top of the C60 aggregate, which makes it have some phase similarities to C60, but also a slight shift toward SubPc phase.

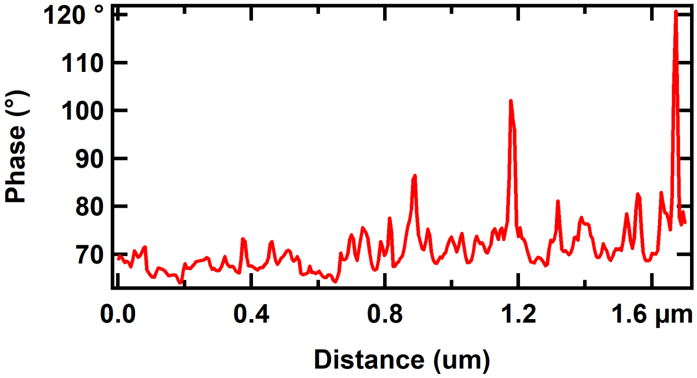

Figure 3.16: Line plot of the phase of the 40:60 sample.

The potential for this scan was similar to that for the bilayer sample, where the scan began in the dark and then halfway through the scan the light was turned on to scan in illumination. We wanted to see the change when the light is turned on in the middle of one of the C60 aggregates, so that is what we did in this test. The potential is shown in Figure 3.17, and the plot of the potential shown in Figure 3.18.

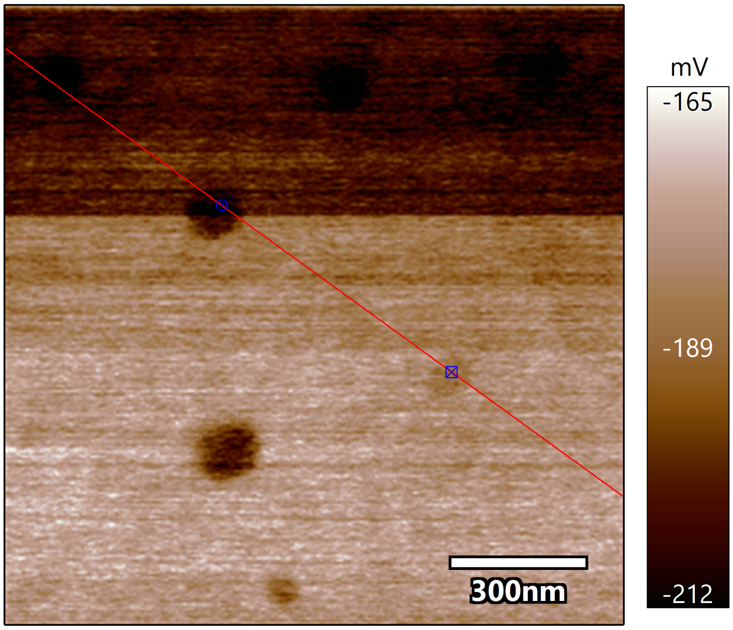

Figure 3.17: Potential of the surface in the dark (bottom half) and under illumination (top half).

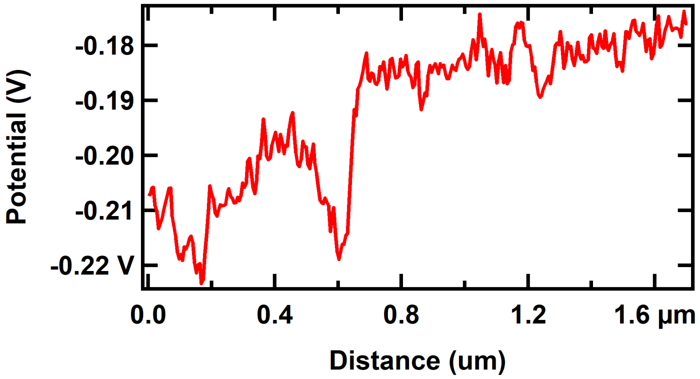

Figure 3.18: Plot of the potential of the surface in the dark (left half) and under illumination (right half).

Similarly to the bilayer sample, the potential shifts toward a positive voltage instead of a negative voltage as expected. The change in voltage is hard to tell in this image between the dark and illuminated scans. Since it was hard to tell the difference between illuminated and dark, we decided to enlarge the scale and focus on a single aggregate of the 40:60 sample after seeing the results of the flattened potential.

Another way to analyze the potential of the sample is to do a flatten order 0 with a mask applied to the darker areas, and see the difference between the aggregates. This potential is shown in Figure 3.19. The difference of when the light was on or off is now unclear in the image, but the plot with the potential gives information about the sample. Figure 3.20 shows a plot of the topography and potential, and it is seen that there is a larger and shorter aggregate with corresponding larger and smaller potential. The difference in potential could be from the difference in height of the aggregates, but could also be from the illuminated or dark scan. The larger aggregate in this case is when the scan was illuminated, and the smaller in the dark. This would then support what we expect to see, that there is a larger shift in potential to be more negative once the sample is under illumination.

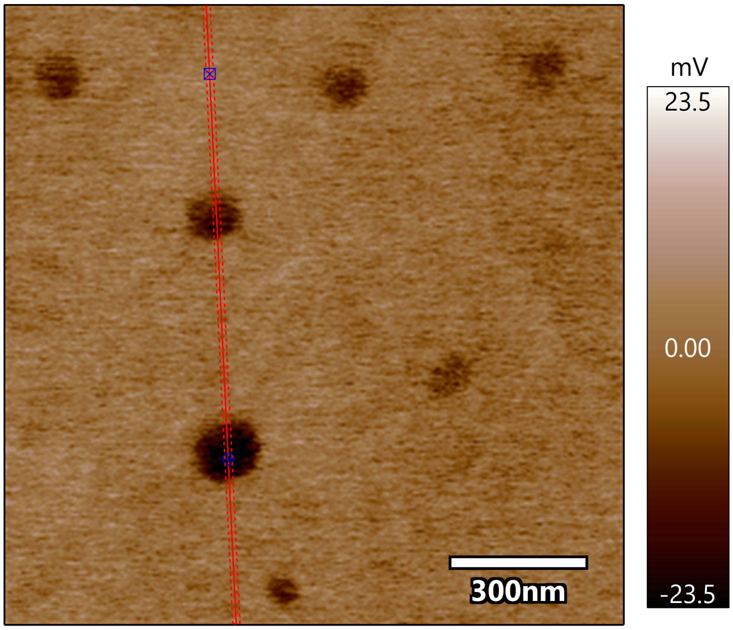

Figure 3.19: Flatten order 0 potential of the surface of the 40:60 sample.

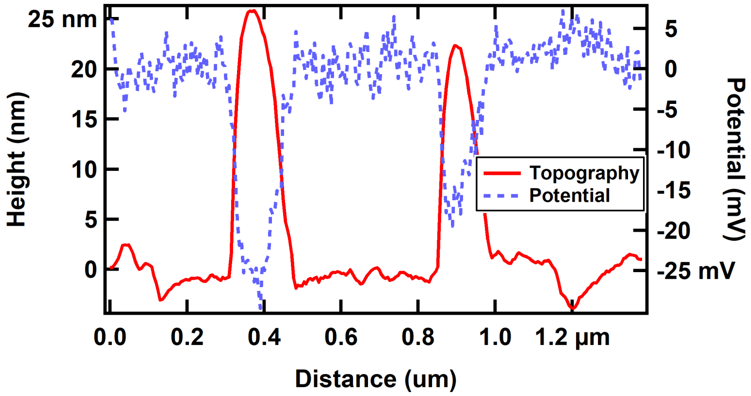

Figure 3.20: Plot of the flatten order 0 potential of the surface of the 40:60 sample.

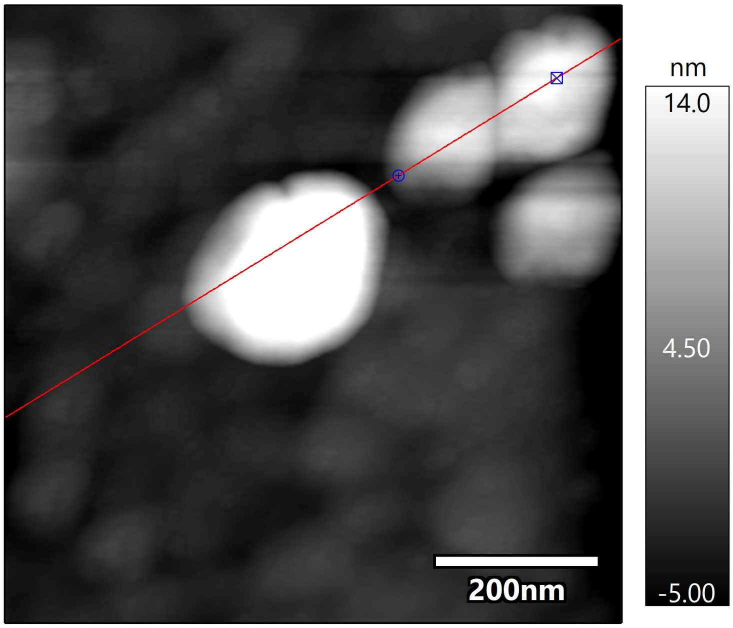

Figure 3.21: Topography of the high-resolution 40:60 sample. Red line indicates where the line plot in Figure 3.14 is taken.

Figure 3.21 shows a topography scan of the 40:60 sample in an enlarged scale, with a scan size of approximately 900 x 900 nm. The plot of the topography along the line is shown in Figure 3.22. In the topography image, it is clear that there is a circular peak which has an elevated height compared to the rest of the surface. This peak measures to be about 25 nm in height, which is taller than the other C60 aggregates we have seen. The two smaller circles also have an increased height of about 15 nm compared to the rest of the sample. The reason for the varying height of these aggregates is from crystallization that occurs while annealing. The combination of coevaporation and annealing could lead to some larger and some smaller aggregates of C60 forming.

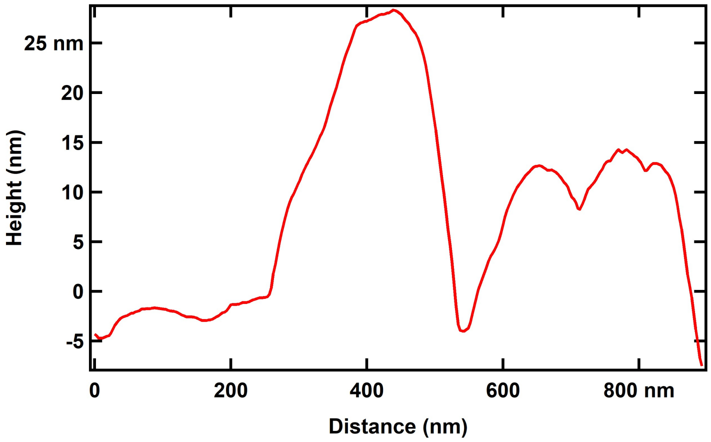

Figure 3.22: Line plot showing the topography of the high-resolution 40:60 sample.

Another option to look at the photovoltage is to see the topography and potential plots stacked on top of each other, to see how the topography can influence the potential. The plots of the high-resolution 40:60 sample is shown in Figure 3.23.

In this plot, it is clear to see that there is a correlation between the topography and the potential of the samples. As the height increases, the potential changes to be more negative. This is because of the C60 aggregates, which are electron acceptors, so their potential shifts to be more negative than the rest of the sample.

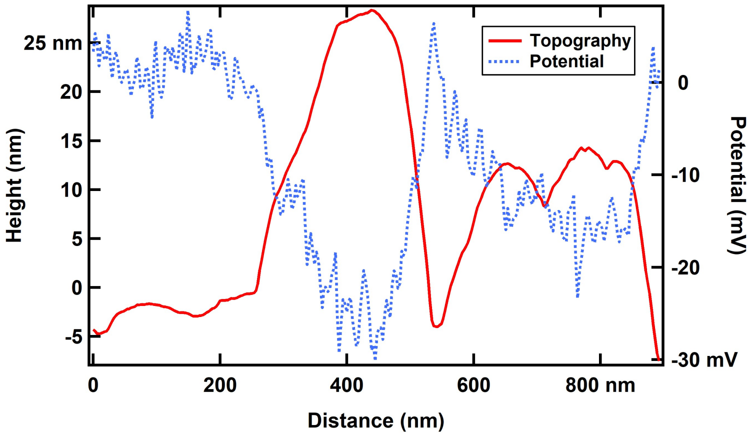

Figure 3.23: Plot of the potential and the topography of the surface of the high-resolution 40:60 sample.

Another test was to take a line plot through both the dark and illuminated sides of a high-resolution image. The topography of the second high-resolution 40:60 sample is shown in Figure 3.24, with the plot of the line showed in Figure 3.25.

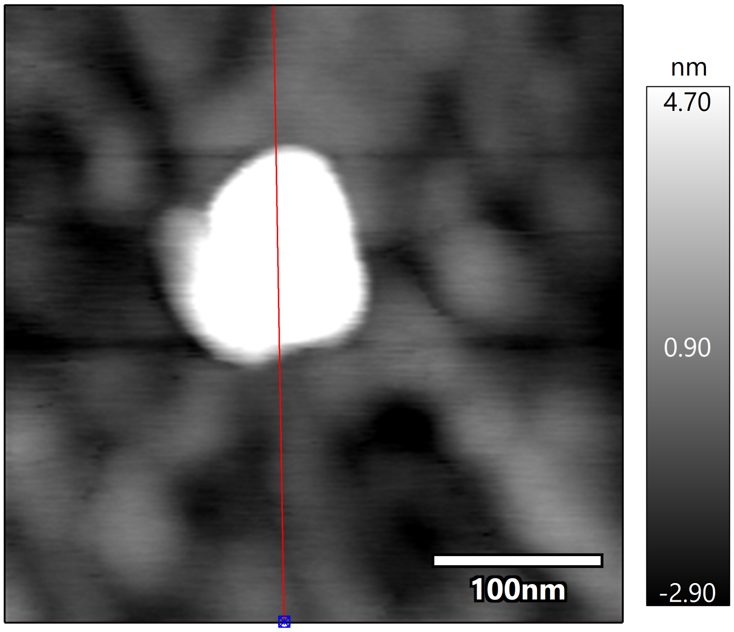

Figure 3.24: Topography of the surface of the second high-resolution 40:60 sample.

In the topography, there is one large aggregate that we have focused on. This aggregate has a height of about 25 nm, as seen in the line plot of the scan. This allows for us to see how

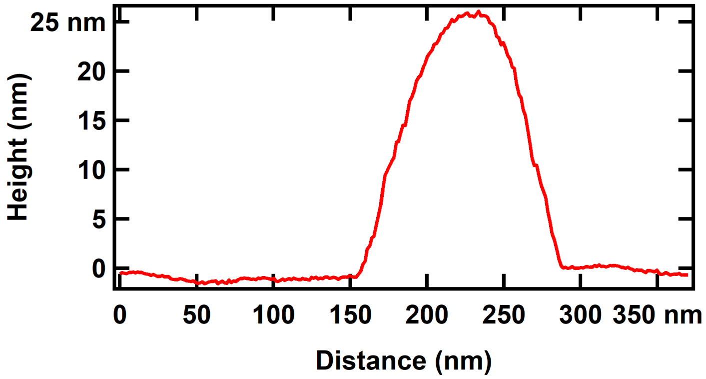

Figure 3.25: Line plot of topography of the surface of the second high-resolution 40:60 sample.

the photovoltage of this C60 aggregate is affected by illumination. The potential is shown in Figure 3.26, with the line plot in Figure 3.27.

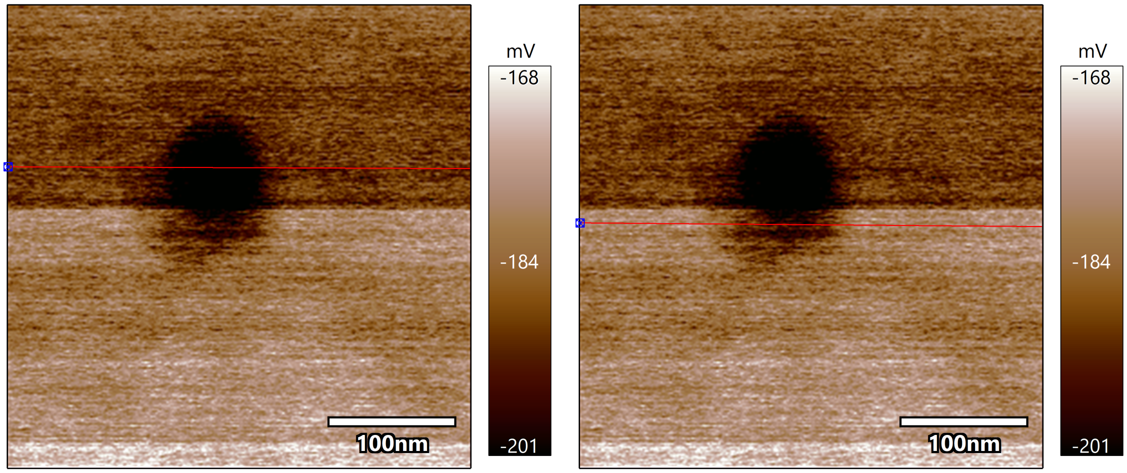

Figure 3.26: Potential over the surface of the second high-resolution 40:60 sample, with lines drawn through the top (left) and bottom (right) for line plots.

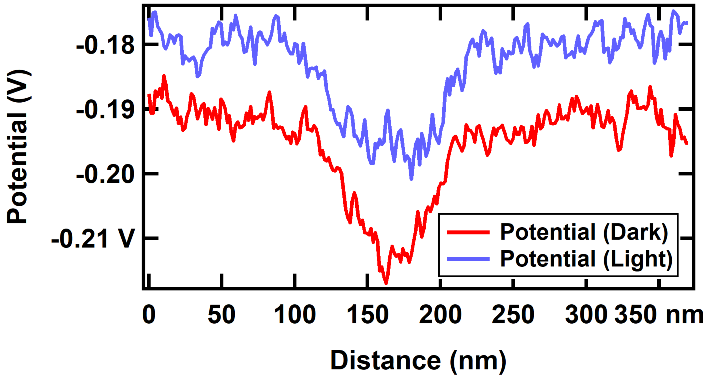

Figure 3.27: Line plot of potential of the surface of the second high-resolution 40:60 sample. The dark potential is in red and the illuminated potential in blue.

From the plot of the potential, it is clear that there is a difference between the illuminated and dark scans. Similarly to the bilayer sample, the contrast between illuminated and in the dark is the opposite of what is expected, though it is promising that there seems to be a greater shift in the slope of the dark potential versus the illuminated potential, instead of the same shift in both of them.

3.4 Discussion of Results

The results were not what we expected to see from these samples. Since the C60 is an acceptor material, when light is shined onto the bilayer or bulk heterojunction the positive charges should be collected through the grounded wire, while the electrons should rest on the surface of the material since there is no top electrode for them to be collected by. This means that the charge on the surface of the sample should have a more negative charge once the light is shined onto it. This is a very interesting case since the opposite was seen, an increase in the potential rather than a decrease. The photovoltage shifting to be more positive under illumination is not the only odd thing that happened during this experiment. When discussing the KPFM procedure with a solar cell expert, Alexi Arango, he mentioned that the shift in voltage should be about 1 volt between the dark and illuminated scans, but this was not the case. The largest voltage shift that was observed was in the bilayer sample, and it was only 30 mV, much less than the expected value.

There are some reasons why these problems could be happening. The first reason could be that the intensity of the light source is not large enough. With the current setup we have, the light source is only able to reach 500 mA of current, which could lead to less photons being absorbed. Next, the ambient environment that the AFM is in could lead to sample damage and charges being collected by H_2O and O_2 molecules in the atmosphere, which would lead to less negative charges on the surface of the sample.

3.5 Summary of Results

To summarize the results, we found that there is the opposite of the expected result when the solar cell samples are illuminated. This could be due to imaging in an ambient environment or the intensity of our light source. The voltage shift is in the positive direction instead of the negative direction, which is an interesting result of this experiment. The bilayer solar cell showed the largest change in potential when exposed to light, which was expected since there is a smaller interface and less chance for recombination of electron-hole pairs to occur. The 40:60 SubPc/C60 bulk heterojunction showed the most promise of the ratios, as there was a higher potential change than that of in the 20:80 bulk heterojunction ratio sample.

Chapter 4:

Conclusion

4.1 Summary of the Research

This research was informative of the SubPc:C60 bulk heterojunction, and how the photovoltage changes when KPFM is done in the dark and under illumination. I was able to learn KPFM techniques which I had not done before, as well as gain fabrication experience with the evaporator when making the half solar cells. Coevaporation was another new technique I learned, and seeing the difference between the bilayer and bulk heterojunction solar cells was informative to understand how the bulk heterojunction solar cell functions differently than a more traditional organic solar cell. The largest difference in potential between the illuminated and dark scans was about 30 mV, and the 40:60 SubPc/C60 bulk heterojunction solar cell showed the most voltage change of the two bulk heterojunction samples.

4.2 Future Work

There are many steps that we want to take for this project in the lab. The first goal is to figure out why the voltage change between the dark and illuminated scans is not at the expected value. We have three main experiments to test- imaging in nitrogen, fabricating and imaging a sample with different materials, and trying a different morphology.

The first experiment to try is to design a new sample holder than can be used for imaging in nitrogen. By allowing the KPFM imaging to happen in nitrogen, it should reduce the amount of ambient factors that could be collecting charges so they don't remain on the surface. This would take a while to set up, as we don't currently have the capability in the lab to image in nitrogen while also shining light on the sample, only one or the other.

The next test involves changing the sample materials entirely, and attempting to replicate a different experiment that has been done. There have been many polymer/C60 or C70 bulk heterojunctions, and testing this instead of a small molecule/C60 blend could prove useful to see if it is the materials that are causing most of the issues that we are seeing. While this could help, it would be interesting if this is the main reason that the bulk heterojunction isn't seeing as large of a photovoltage change as we are expecting since there have been full solar cells made using a SubPc/C60 heterojunction that have worked at the expected efficiency.

Lastly, another test could be to continue to change the ratio of materials to see if that impacts the photovoltage measurements. One suggestion is to deposit a pristine layer of SubPc on top of the MoO_3, and then coevaporate the SubPc and C60 materials on top of it. This could allow for there to be more of a barrier between the MoO_3 and bulk heterojunction, in case this is the reason that we are not seeing the charge we are expecting. Changing the ratio of SubPc and C60 is another option, since only the 20:80 and 40:60 ratios of SubPc/C60 have been tested. An interesting test could be to reverse the ratios, having a 80:20 and 60:40 SubPc/C60 ratio sample and seeing how this changes the photovoltage measurements.

References

[1] Maka, Ali O M and Alabid, Jamal M "Solar energy technology and its roles in sustainable development", *Clean Energy* 6, 3: 476-483 (2022).

[2] Pandey, Richa and Holmes, Russell J. "Characterizing the charge collection efficiency in bulk heterojunction organic photovoltaic cells", *Applied Physics Letters* 100, 8 (2012).

[3] Liu, Kerui and Jiang, Yuanyuan and Ran, Guangliu and Liu, Feng and Zhang, Wenkai and Zhu, Xiaozhang "19.7% efficiency binary organic solar cells achieved by selective core fluorination of nonfullerene electron acceptors", *Joule* 8, 3: 835-851 (2024).

[4] Ostroverkhova, Oksana "Organic Optoelectronic Materials: Mechanisms and Applications", *American Chemical Society* 116, 22 (2016).

[5] Khunchan, S and Wiengmoon, B. "Method to determine the single curve IV characteristic parameter of solar cell", *Journal of Physics: Conference Series*, 1144, 1: 012012 (2018).

[6] Wood, Dawn "Quantitative electrical characterisation of organic semiconductors by atomic force microscopy", *University of Warwick* (2017).

[7] Maturová, Klára and Kemerink, Martijn and Wienk, Martijn M and Charrier, Dimitri SH and Janssen, René AJ. "Scanning Kelvin probe microscopy on bulk heterojunction polymer blends," *Advanced Functional Materials*, 19, 9: 1379-1386 (2009).

[8] Zhang, Qian and Cohen, Sidney R and Rosenhek-Goldian, Irit and Amgar, Daniel and Bar-Elli, Omri and Tsarfati, Yael and Bendikov, Tatyana and Shimon, Linda JW and Feldman, Yishay and Iron, Mark A and others. "A Nanoscopic View of Photoinduced Charge Transfer in Organic Nanocrystalline Heterojunctions," *The Journal of Physical Chemistry C*, 123, 41: 25031-25041 (2019).

[9] Chiesa, Marco and Bürgi, Lukas and Kim, Ji-Seon and Shikler, Rafi and Friend, Richard H. and Sirringhaus, Henning "Correlation between Surface Photovoltage and Blend Morphology in Polyfluorene-Based Photodiodes", *Nano Letters* 5, 4: 559-563 (2004).

[10] Fengler, S. and Dittrich, Th. and Rusu, M. "Electronic transitions and band offsets in C60:SubPc and C60:MgPc on MoO3 studied by modulated surface photovoltage spectroscopy", *Journal of Applied Physics* 118, 3 (2015).

[11] Chidichimo, Giuseppe and Luigi, Filippelli, “Organic Solar Cells: Problems and Perspectives”, *International Journal of Photoenergy*, (2010).

[12] Gao, Yuan and Jin, Fangming and Li, Wenlian and Su, Zisheng and Chu, Bei and Wang, Junbo and Zhao, Haifeng and Wu, Hairuo and Liu, Chengyuan and Hou, Fuhua and others “Highly efficient organic tandem solar cell with a SubPc interlayer based on TAPC: C70 bulk heterojunction”, *Scientific Reports* 6, 1: 23916 (2016).

[13] Shang, Yuchen and Liu, Zhaodong and Dong, Jiajun and Yao, Mingguang and Yang, Zhenxing and Li, Quanjun and Zhai, Chunguang and Shen, Fangren and Hou, Xuyuan and Wang, Lin and others “Ultrahard bulk amorphous carbon from collapsed fullerene”, *Nature* 599, 7886: 599-604 (2021).

[14] Berné, Olivier and Montillaud, J. and Mulas, Giacomo and Joblin, Christine “30 years of cosmic fullerenes”, *Journal of Chemical Theory and Computation*, (2015).

[15] Sadewasser, Sascha and Glatzel, Thilo “Kelvin Probe Force Microscopy: From Single Charge Detection to Device Characterization”, *Springer* 65, 3-25 (2018).

[16] Axt, Amelie and Hermes, Ilka M and Bergmann, Victor W and Tausendpfund, Niklas and Weber, Stefan AL “Know your full potential: Quantitative Kelvin probe force microscopy on nanoscale electrical devices”, *Beilstein Journal of Nanotechnology* 9, 1: 1809-1819 (2018).

[17] Si, Haonan and Zhao, Xuan and Zhang, Zheng and Liao, Qingliang and Zhang, Yue “Low-temperature electron-transporting materials for perovskite solar cells: Fundamentals, progress, and outlook”, *Coordination Chemistry Reviews* 500, 215502 (2023).

[18] Kim, Jinhyun and Yim, Sanggyu “Influence of surface morphology evolution of SubPc layers on the performance of SubPc/C60 organic photovoltaic cells”, *Applied Physics Letters* 99, 19 (2011).

[19] Mutolo, Kristin L. and Mayo, Elizabeth I. and Rand, Barry P. and Forrest, Stephen R. and Thompson, Mark E. “Enhanced Open-Circuit voltage in Subphthalocyanine/C60 organic photovoltaic cells”, *Journal of the American Chemical Society* 128, 25: 8108-8109 (2006).

[20] Peet, Jeffrey and Heeger, Alan J. and Bazan, Guillermo C. “’Plastic’ solar cells: Self-Assembly of bulk heterojunction nanomaterials by spontaneous phase separation”, *Accounts of Chemical Research* 42, 11: 1700-1708 (2009).

[21] Shahiduzzaman, Md. and Yonezawa, Kyosuke and Yamamoto, Kohei and Ripolles, Teresa S. and Karakawa, Makoto and Kuwabara, Takayuki and Takahashi, Kohshin and Hayase, Shuzi and Taima, Tetsuya “Improved reproducibility and intercalation control of efficient planar inorganic perovskite solar cells by simple alternate vacuum deposition of PBI2 and CSI”, *ACS Omega* 2, 8: 4464-4469 (2017).